

Development of a Multiphase Beryllium Equation of State and Physics-based Variations

Published as part of *The Journal of Physical Chemistry* virtual special issue "Emily A. Carter Festschrift".

Christine J. Wu,* Philip C. Myint, John E. Pask, Carrie J. Prisbrey, Alfredo A. Correa, Phanish Suryanarayana, and Joel B. Varley



Cite This: *J. Phys. Chem. A* 2021, 125, 1610–1636



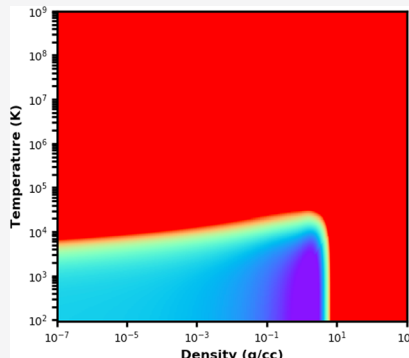
Read Online

ACCESS |

 Metrics & More

 Article Recommendations

ABSTRACT: We construct a family of beryllium (Be) multiphase equation of state (EOS) models that consists of a baseline ("optimal") EOS and variations on the baseline to account for physics-based uncertainties. The Be baseline EOS is constructed to reproduce a set of self-consistent data and theory including known phase boundaries, the principal Hugoniot, isobars, and isotherms from diamond-anvil cell experiments. Three phases are considered, including the known hexagonal closed-packed (hcp) phase, the liquid, and the theoretically predicted high-pressure body-centered cubic (bcc) phase. Since both the high-temperature liquid and high-pressure bcc phases lack any experimental data, we carry out *ab initio* density functional theory (DFT) calculations to obtain new information about the EOS properties for these two regions. At extremely high temperature conditions (>87 eV), DFT-based quantum molecular dynamics simulations are performed for multiple liquid densities using the state-of-the-art Spectral Quadrature methodology in order to validate our selected models for the ion- and electron-thermal free energies of the liquid. We have also performed DFT simulations of hcp and bcc with different exchange-correlation functionals to examine their impact on bcc compressibility, which bound the hcp–bcc transition pressure to within 4 ± 0.5 Mbar. Our baseline EOS predicts the first density maximum along the Hugoniot to be 4.4-fold in compression, while the hcp–bcc–liquid triple-point pressure is predicted to be at 2.25 Mbar. In addition to the baseline EOS, we have generated eight variations to accommodate multiple sources of potential uncertainties such as (1) the choice of free-energy models, (2) differences in theoretical treatments, (3) experimental uncertainties, and (4) lack of information. These variations are designed to provide a reasonable representation of nonstatistical uncertainties for the Be EOS and may be used to assess its sensitivity to different inertial-confinement fusion capsule designs.



INTRODUCTION

Beryllium (Be) is a material with highly desirable properties and is used in a wide range of applications that require stability at high temperatures and pressures, despite being classified as a hazardous material. It is a lightweight, low-density metal (1.85 g/cm^3 at ambient conditions) that also happens to be exceptionally strong. Unlike most metals, its shear modulus actually exceeds its bulk modulus.^{1,2} Be possesses one of the largest ambient bulk and longitudinal sound velocities among metallic compounds due to its extraordinary modulus-to-density ratio. Moreover, it exhibits a broad thermal stability with a melting point of 1560 K and substantial resistance to oxidization.³ Because of these favorable traits, Be has been considered as a potential capsule material for inertial-confinement-fusion (ICF) applications.⁴ Hydrodynamic simulations of ICF are frequently used to model the capsule behavior under the intense compression initiated by laser pulses. This requires a Be equation of state (EOS) that can

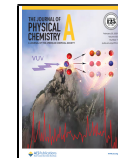
accurately describe material response under compression and heating.

Over the years, several Be EOSs have been developed. Each uses varying sets of experimental and/or theoretical data, and they differ in the choice of models, data-fitting schemes, and simplifications/approximations. Thus, each Be EOS is unique, and for many properties or conditions, predictions can vary from one EOS to another. Early EOSs, such as LEOS 40 (L40) developed by Young et al.⁵ at Lawrence Livermore National Laboratory (LLNL) and SESAME 2023 (S2023) at Los Alamos National Laboratory⁶ are built primarily from

Received: October 30, 2020

Revised: January 15, 2021

Published: February 15, 2021



experimental data. Rudin and Johnson later created S2024,⁷ which incorporated *ab initio* density functional theory (DFT) information in a multiphase treatment. In 2009, Benedict et al.⁸ built the first LLNL multiphase Be EOS in the density range of $1 \text{ g/cm}^3 < \rho < 10 \text{ g/cm}^3$, which is based on DFT simulations. Shortly after, Robert et al.⁹ reported another commonly cited Be EOS that utilizes a similar but independent DFT approach from Benedict et al., as well as different free-energy models. In 2017, Ding and Hu¹⁰ reported a direct DFT-based EOS starting at 2000 K for Be liquid. This EOS was populated with energies and pressures obtained from quantum molecular dynamics (QMD) below $2.5 \times 10^5 \text{ K}$ and orbital-free QMD above $2.5 \times 10^5 \text{ K}$. The drawback of not using free-energy models is that the required thermodynamic consistency between the *ab initio* energies and pressures is not guaranteed. In addition, their *ab initio* results overpredict the Hugoniot pressure by more than 10% for some regimes. This is not surprising, since DFT results are sensitive to computational details, and agreement with experiments needs to be conscientiously certified. Adopting a different choice of exchange–correlation functional (XCF), pseudopotential, thermostat treatment, or simulation cell size can lead to different results and therefore contribute to the discrepancies seen in *ab initio* results.

As a segue to further discussion on EOS uncertainties, it is worth noting that even to this day, the Be phase diagram has still not been well established. In particular, the stability field of the body-centered cubic (bcc) phase, which has been suggested to exist in two separate regions—one at low pressure and another at high pressure—is a subject of active debate. For the purposes of this paper, we use “ β -Be” to refer to the low-pressure bcc phase and “bcc” to refer to the high-pressure phase. At ambient conditions, Be exists as a hexagonally closed-packed (hcp) structure known as α -Be. Early experiments report that heating α -Be at low pressures creates a new β -Be structure just before melting. The observed β -Be polymorph was interpreted as having a body-centered cubic structure and existing in a narrow region of phase space approximately 30 K below the melting temperature.^{11–15} These results have garnered a considerable amount of interest from the EOS community as the body-centered cubic lattice is known to be stable at high temperatures due to strong anharmonicity.^{8,9,16,17} Unfortunately, the existence of β -Be below the melting temperature was not observed in several modern diamond-anvil cell (DAC) experiments.^{18,19} One hypothesis that has been presented to explain this controversy is that the Be samples used in early experiments may have contained unknown impurities. On the theoretical side, DFT calculations have indicated that the bcc phase of Be is likely mechanically unstable at low temperatures.⁸ Recently, Lu et al.²⁰ investigated the existence of a Be bcc phase prior to melting using a hybrid free-energy method, which combines both QMD and lattice dynamics to account for anharmonic effects. Their results show that the bcc phase becomes more stable than hcp phase for temperatures above 1480 K and pressures less than 11 GPa. However, they do not address liquid stability relative to the bcc phase, which is necessary to confirm the existence of bcc prior to melting.

Given the inconclusive nature of this hcp– β -Be phase transition and the narrow pressure and temperature range that the β -Be structure potentially resides in, we do not expect it to be important for ICF applications. For these reasons, we have not included the β -Be phase in our EOS construction,

similar to previous multiphase EOSs.^{7–9} However, since the high-pressure bcc phase resides in a region of phase space that is potentially relevant to ICF applications, we have included it in our Be EOS construction, despite the fact that it has been observed only in theoretical studies. Thus, our EOS features three phases: hcp, (high-pressure) bcc, and liquid. We note that to keep the nomenclature simple in this study, we use “liquid” as a catchall to refer to any of the fluid phases that collectively span the very wide temperature (10^2 – 10^9 K) and density (10^{-7} – 10^3 g/cm^3) ranges over which we intend our EOS to be applicable. Therefore, not only does “liquid” represent the actual liquid phase, it also includes vapor, supercritical fluid, warm-dense matter, and ionized plasma. Following a naming convention widely used in the high-pressure EOS community, we refer to a wide-ranging EOS such as ours as being a “global” EOS.

In addition to the theoretical (e.g., choice of XCF) uncertainties discussed above and the controversy over the phase diagram, there are numerous experimental uncertainties and disagreements for other measurements on Be. For instance, we will show that there are discrepancies regarding the compressibility of the hcp phase and the behavior of the shock Hugoniot in the liquid regime, as well as a lack of data along the melt curve and high-temperature isotherms. Therefore, before constructing the EOS, we must first carefully analyze the available data in order to select a set of experimental and theoretical constraints that are consistent with each other and to thoroughly understand key uncertainties that could impact its accuracy.

Considering the aforementioned controversies regarding the properties of Be, a question naturally arises as to how one should construct the best EOS while accounting for all existing EOS uncertainties. Typically, a single “optimal” EOS is delivered that tries to best reproduce a chosen set of experimental and theoretical constraints based on the reliability of the data, level of theory, or choice of model. In this work, we propose a new EOS delivery paradigm that produces a family of EOS models, which includes a “baseline” (which we deem to be the optimal model) and a set of other EOSs (also known as “variations”) that deviates from the baseline to account for known physics-based uncertainties. This approach is analogous to using a set of interatomic potentials instead of just one particular potential in classical molecular dynamics (MD) simulations. To further improve the fidelity of the baseline EOS, we have performed additional *ab initio* DFT calculations for the regions that lack data, such as the high-pressure bcc and extremely high-temperature liquid regimes. We have constructed eight EOS variations to address key controversies arising from four different types of uncertainties: (1) ambiguities in the choice of free-energy models, (2) constraints imposed by various theoretical predictions, (3) experimental uncertainties, and (4) lack of data in certain conditions. We intend to only cover possibilities that are expected to be impactful for ICF applications. Statistical treatment of random errors²¹ from experimental measurements are outside the scope of this work. Our physics-based approach could, however, complement these statistical approaches in future EOS development of other materials.

We have developed nine EOSs in total, which includes the baseline that we refer to as L42 and the eight variations which we label as L9421–L9428. The rest of this paper is arranged as follows. In “EOS Methodology: Models, Theory, and Construction” (for short, we refer to this as the *Methodology*

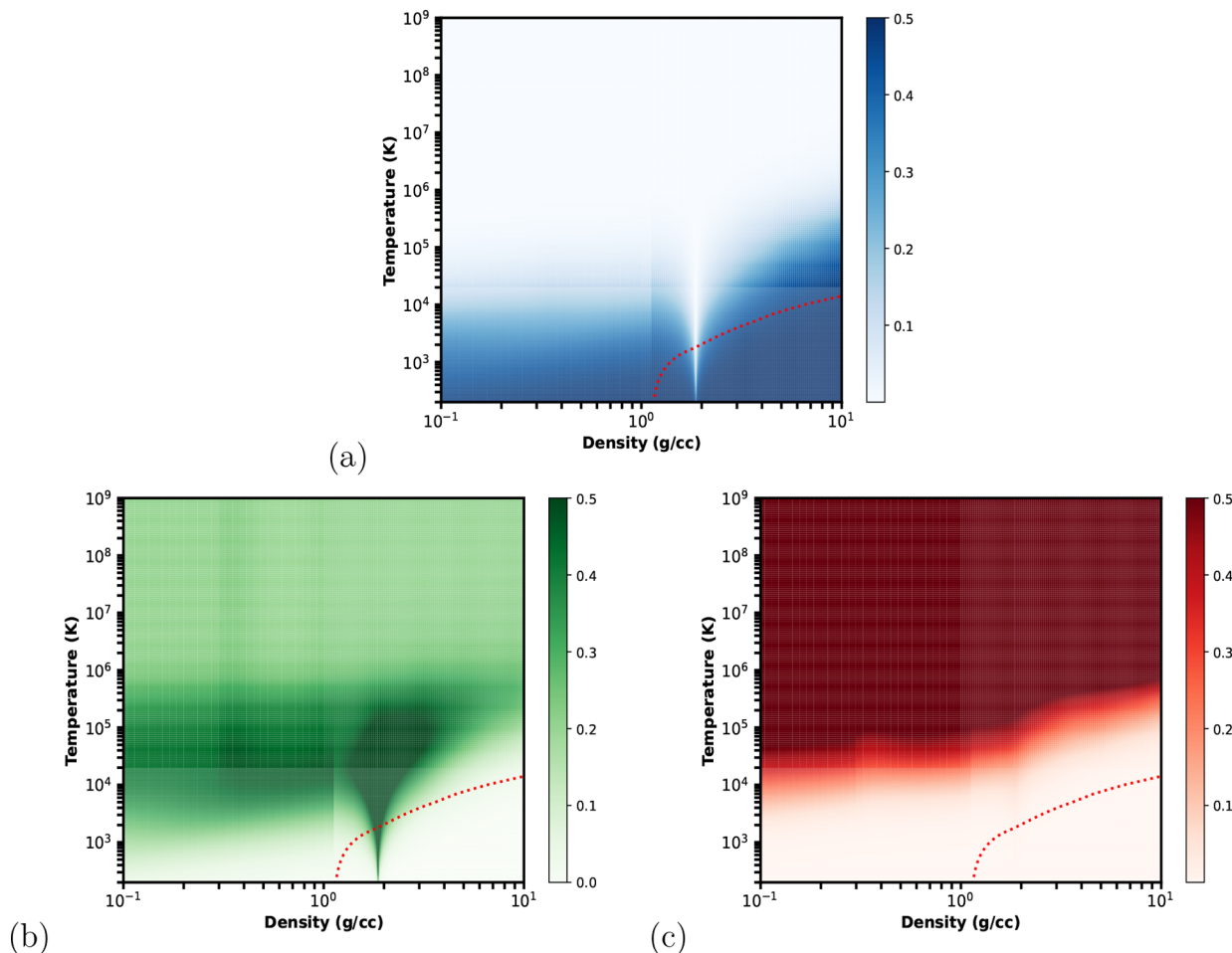


Figure 1. Comparison of the three different contributions to the total sum of pressure magnitudes $|P| = |P_{\text{cold}}| + |P_{\text{ion}}| + |P_{\text{electron}}|$ in our L42 Be EOS. The figures depict, for a given density and temperature, the fraction of the total pressure made by each contribution: (a) cold pressure $|P_{\text{cold}}|/|P|$; (b) ion-thermal pressure $|P_{\text{ion}}|/|P|$; (c) electron-thermal pressure $|P_{\text{electron}}|/|P|$. The dashed curve in red illustrates the melt curve. We have restricted the density range of this plot to be 0.1 – 10 g/cm 3 for the purposes of visual clarity.

section), we describe the free-energy models used in our L42 baseline and details on the numerical implementation of these models. In “*Ab Initio* Quantum Calculations” (*Ab Initio* section), we discuss first-principles DFT/QMD calculations we have performed in regions where there is an absence of experimental data. These calculations help to constrain or validate the models and shed light on the behavior of Be at extreme pressures and temperatures. We then proceed to “L42 baseline results and discussion” (*Baseline* section), which provides phase-specific model parameters and illustrates key comparisons between L42 and a self-consistent set of experimental and theoretical data. In addition, the *Baseline* section makes informed predictions on disputed properties like the hcp–bcc phase boundary and the hcp–bcc–liquid triple point. We do the same type of comparisons for each of the eight variations in “EOS variations results and discussion” (*Variations* section). We conclude with a summary of this study and describe how our study informs future EOS experiments on Be.

■ EOS METHODOLOGY: MODELS, THEORY, AND CONSTRUCTION

This section describes the methodology behind the construction of our multiphase EOSs. Our ultimate goal is to obtain a set of phase-specific free-energy models to accurately

represent Be properties and replicate known features of the Be phase diagram. In this *Methodology* section, we first present the different phenomenological free-energy models used to construct our L42 baseline EOS. Each of the eight variations we present later on deviate from this baseline in only one particular aspect (e.g., switching out one model with another). We have built all of our EOSs using MEOS, which is a newly developed LLNL object-oriented code that enables fast multiphase EOS construction and the flexibility of implementing new free-energy models in a straightforward, timely manner. MEOS is a significant step forward from the QEoS/XEoS methodology²² that has been LLNL’s workhorse EOS scheme for decades. QEoS/XEoS is not a multiphase scheme and is based on one set of model choices [e.g., the Cowan model^{22,23} to describe the liquid phase and a Thomas–Fermi (TF) model for the electronic contributions to the free energy, both of which we describe below]. MEOS provides additional capabilities that are necessary for applications that demand higher accuracy. It is a multiphase framework that allows for the inclusion of phase-specific physics and adoption of more accurate free-energy models, such as the Cell model^{24,25} for liquid and Purgatorio^{26,27} for electronic ionization and excitation processes that become prominent at high temperatures and pressures. The implementation of Purgatorio and construction of phase boundaries

requires overcoming certain numerical difficulties, and the practical ways we have done this in MEOS are described near the end of this *Methodology* section.

Baseline EOS Models. Overview. In this study, each phase is modeled with a separate function $F = F(T, V)$ that represents the Helmholtz energy of that phase in terms of temperature T and volume V . We adopt the formalism commonly used in high-pressure science in which F is subsequently divided into the three contributions below:

$$F(T, V) = F_{\text{cold}}(V) + F_{\text{ion}}(T, V) + F_{\text{electron}}(T, V) \quad (1)$$

where the cold energy $F_{\text{cold}}(V)$ designates the energy of the phase at 0 K, the ion-thermal free energy $F_{\text{ion}}(T, V)$ accounts for the thermal motion of the nuclei (e.g., lattice vibrations if the phase in question is a solid), and the electron-thermal free energy $F_{\text{electron}}(T, V)$ reflects electronic excitations and ionization processes that become prominent at high temperatures and pressures. Other thermodynamic properties, like the pressure P , entropy S , and internal energy E , are obtained by taking one or more derivatives of F with respect to T and/or V .

In general, each of the three free-energy contributions has its own temperature-density regime where it dominates the overall behavior (Figure 1). The cold contribution is most prominent at low temperatures and high densities but becomes less important with increasing temperature as thermal excitations of the nuclei and the electrons become more pronounced. The electron-thermal term becomes the leading contributor at high temperatures, especially in the warm-dense-matter and plasma regimes. The ion-thermal term is most influential in regions where motion of the nuclei is prominent and the cold and electron-thermal contributions are small. One of these regions corresponds to low-density conditions where the system exists as a gas, but it is also important in certain condensed-phase conditions, particularly those at higher temperatures near ambient density where the cold-pressure contribution is small. We note that since Be is a low-Z material (its atomic number $Z = 4$), the ion-thermal term of Be makes a non-negligible contribution [e.g., $1/(1 + Z) = 20\%$] even at high temperatures where the electrons are expected to be fully ionized.

Cold Energy. The cold energy $F_{\text{cold}}(V)$ of a phase is largely a reflection of its potential energy in the ground-state electronic configuration and excludes thermal motion of the nuclei, though it does include the zero-point energy in our EOS construction. We have found that a single analytical expression for $F_{\text{cold}}(V)$ cannot adequately cover the enormous range of densities for our global EOS (10^{-7} – 10^3 g/cm³) because the behavior of a material over these 10 orders of magnitude is extremely varied. For example, the cold curve is monotonic in pressure above a particular density, but in order for it to properly account for solid in tension and go to the ideal-gas limit, the pressure must be negative and nonmonotonic in some portion of the low-density (expansion) region.

Since a single analytical function is not sufficient for our purposes, we represent the cold curve as a series of cubic splines (specifically, the “bimond” scheme²⁸ based on cubic Hermite polynomials) that smoothly connect three domains in density ρ : (1) ideal-gas limit (e.g., $\rho < 10^{-3}$ g/cm³); (2) conditions near ambient density up to moderate compression (this intermediate domain is often the one that is examined in DAC studies and is the one we pay most attention to in this study); (3) highly compressed states (up to 10^3 g/cm³) for which we use the computed cold curve from the Purgator-

io^{26,27} averaged-atom-in jellium model that we describe later. Although the cold curve is ultimately represented by splines defined over a nonuniformly spaced set of control points in ρ , a piecewise-smoothing procedure (fitted by localized polynomials) over multiple regions is applied to reduce some of the numerical noise. This numerical representation greatly improves our ability to perform local optimization. The deployment of splines ensures the continuity of the cold energy and the first two derivatives of this quantity (the cold pressure and bulk modulus, respectively). We have verified that other comparable interpolation schemes²⁸ yield similar results. Nevertheless, our future treatment could be improved by adopting the spline-based method developed by Brown et al.,^{29,30} which allows for continuity of derivatives up to any arbitrary order and more sophisticated smoothing (regularization) techniques.

For comparison purposes with other EOSs or experimental (DAC) data, it is possible to fit the cold curve in the neighborhood of a relatively narrow range of densities near ambient conditions to an analytical function like the well-known Vinet–Rose equation³¹ given below:

$$\begin{aligned} F^{\text{Vinet}}(V) &= E_0 + \frac{4V_0B_0}{(B'_0 - 1)^2} [1 - (1 + X) \exp(-X)] \\ X &= \frac{3}{2}(B'_0 - 1) \left[\left(\frac{V}{V_0} \right)^{1/3} - 1 \right] \end{aligned} \quad (2)$$

where V_0 is the volume that we would obtain at zero pressure and 0 K, B_0 is the optimized value of the isothermal bulk modulus at V_0 , B'_0 is the pressure derivative of B_0 at V_0 , and E_0 is the internal energy of the phase at V_0 .

Ion-Thermal Free Energy. In all of our EOSs, we have used two different types of ion-thermal free-energy models: one type for each of the solid phases and another type for the liquid. The ion-thermal free energy $F_{\text{ion}}(T, V)$ of the hcp and bcc solid phases is based on the well-known Debye model. According to this model, the Helmholtz energy on a per-atom basis is

$$\begin{aligned} F^{\text{Debye}}(T, V) &= k_B \frac{9\theta(V)}{8} + k_B \left\{ 3T \ln \left\{ 1 - \exp \left[-\frac{\theta(V)}{T} \right] \right\} \right. \\ &\quad \left. - T \mathcal{D} \left[\frac{\theta(V)}{T} \right] \right\} \end{aligned} \quad (3)$$

where $\theta(V)$ is the Debye temperature and the Debye integral is defined as $\mathcal{D}(y) = (3/y^3)(\int_0^y x^3 / [\exp(x) - 1] dx)$. The Debye model can be derived by representing the solid as a collection of quantum harmonic oscillators where the phonon density of states (PDOS) is proportional to the square of the vibrational frequencies.³² This model correctly reproduces the T^3 decay in the ion-thermal contribution to the heat capacity for $T \rightarrow 0$, and at the same time it also recovers the Dulong–Petit limit at high temperatures. The one key parameter in this model is the Debye temperature θ , which is related to the maximum allowed cutoff frequency that is needed to properly set the total number of vibrational modes in the solid. The value of θ is often determined by an optimization procedure to reproduce chosen constraints that can vary in their types and temperature conditions. For example, the Debye temperature that is required to reproduce low-temperature data, such as ultrasonic measurements, is typically different from those obtained by

fitting to high-temperature data, such as entropy measurements. In constructing our EOS, we have followed previous EOS approaches in which the Debye temperature is used as a tuning parameter to best fit experimental entropy data (e.g., for hcp and liquid) or to match the full quasiharmonic free energy computed from the *ab initio* PDOS (e.g., for bcc) at high temperatures.⁸

A closely related quantity to θ is the Grüneisen parameter $\gamma(V) = -d \ln \theta / d \ln V$, which represents the logarithmic derivative of Debye temperature θ as a function of volume. The Grüneisen parameter γ is modeled in our study with a series of splines whose coefficients are adjusted to reproduce experimental and/or theoretical data. Within a limited density range, it is sometimes possible to fit the resulting $\gamma(V)$ curves to a polynomial in V , as reported in other studies.⁸ The ion-thermal free energy of a solid phase in our EOS is obtained by subtracting the zero-point energy term $9k_B\theta(V)/8$ from the Debye free energy so that

$$\begin{aligned} F_{\text{ion}}^{\text{Debye}}(T, V) &= k_B \left[3T \ln \left\{ 1 - \exp \left[-\frac{\theta(V)}{T} \right] \right\} \right. \\ &\quad \left. - T \mathcal{D} \left[\frac{\theta(V)}{T} \right] \right] \end{aligned} \quad (4)$$

The zero-point energy is instead implicitly included in the cold energy $F_{\text{cold}}(V)$, and by separating the different energy terms in this manner we are able to ensure that $F_{\text{ion}}^{\text{Debye}}(T = 0, V) = 0$ for all V .

To model the ion-thermal free energy of the liquid phase in L42, we use the Cell model developed recently by Correa et al.^{24,25} To motivate their model, Correa et al. first demonstrate that the free energy of the Mie–Grüneisen model, which is the high-temperature limit of the Debye model for a solid, can be derived from the classical partition function of a monatomic particle subjected to a harmonic three-dimensional potential. In this partition function, the configurational integral of the harmonic potential extends over all space. In order to more realistically model a liquid, this potential is modified with a confinement boundary such that the motion of a liquid ion is limited to a finite spherical cell of radius R , hence the name of the model. The resulting potential surface has two distinct profiles: a half-sphere for lower-energy modes that reside within the harmonic well and a particle-in-a-cylinder model (the cylindrical analogue of the infinite-square well) of diameter $2R$ for higher-energy modes. After carrying out the integration of the partition function with this potential, Correa et al. obtain the Helmholtz-energy expression (again on a per-atom basis)

$$\begin{aligned} F^{\text{Cell}}(T, V) &= F^{\text{harm}}(T, V) \\ &\quad - k_B T \ln \left[\operatorname{erf} \left(\sqrt{\frac{T^*}{T}} \right) \right. \\ &\quad \left. - \frac{2}{\sqrt{\pi}} \sqrt{\frac{T^*}{T}} \exp \left(-\frac{T^*}{T} \right) \right] \end{aligned} \quad (5)$$

where $\operatorname{erf}(x)$ is the error function, and the characteristic temperature scale T^* is given by

$$k_B T^*(V) = \frac{mk_B^2 \theta(V)^2 R(V)^2}{2\hbar^2} \quad (6)$$

Here, \hbar is the Dirac constant, and we have explicitly noted the volume/density-dependent nature of θ and R . The first term in eq 5, $F^{\text{harm}}(T, V)$, represents the Mie–Grüneisen free energy $-3k_B T \ln[\theta(V)/T]$, which has an internal energy E_{ion} and heat capacity $C_{V,\text{ion}}$ of $3k_B/T/\text{atom}$ and $3k_B/\text{atom}$, respectively. Thus, the second term in square brackets in eq 5 may be viewed as a correction on the Mie–Grüneisen model that one obtains by imposing a limit R on the cell radius. This correction term becomes prominent only at high temperatures. It ensures that the ion-thermal contribution to the heat capacity decreases from the Dulong–Petit value of $3 k_B/\text{atom}$ to the ideal-gas value of $3/2 k_B/\text{atom}$ at high temperatures where $T \gg T^*$ in the following asymptotic manner:²⁴

$$C_{V,\text{ion}} = \frac{3k_B}{2} + \frac{12}{175} k_B \left(\frac{T^*}{T} \right)^2 + \dots \quad \text{for } T \gg T^* \quad (7)$$

Moreover, Correa et al.²⁴ demonstrate that in order for the ion-thermal pressure P_{ion} and entropy S_{ion} to approach their ideal-gas values in the high-temperature $T \gg T^*$ limit, the volume dependence of R must follow $R = [3V/4\pi]^{1/3}$ so that from eq 6, we have

$$k_B T^*(V) = \frac{mk_B^2 \theta(V)^2 [3V/4\pi]^{2/3}}{2\hbar^2} \quad (8)$$

Strictly speaking, an extra factor of $e = \exp(1)$ is needed in this expression to reach the ideal-gas limit (otherwise, it deviates slightly from this limit), but following previous work,²⁵ we omit this factor since doing so yields improved agreement with experiments.

In L42, the ion-thermal free energy of the liquid is given by the Cell model as described above, with the exception that we replace the Mie–Grüneisen term (F^{harm}) with a Debye term ($F_{\text{ion}}^{\text{Debye}}$ defined by eq 4), so that

$$\begin{aligned} F_{\text{ion}}^{\text{liquid}}(T, V) &= F_{\text{ion}}^{\text{Debye}}(T, V) \\ &\quad - k_B T \ln \left[\operatorname{erf} \left(\sqrt{\frac{T^*}{T}} \right) \right. \\ &\quad \left. - \frac{2}{\sqrt{\pi}} \sqrt{\frac{T^*}{T}} \exp \left(-\frac{T^*}{T} \right) \right] \end{aligned} \quad (9)$$

This modification was, in fact, suggested by Correa et al.²⁴ and offers greater flexibility in modeling solid–liquid transitions because, unlike in the Mie–Grüneisen model, $C_{V,\text{ion}}$ is not fixed to $3 k_B/\text{atom}$ in the Debye model. Importantly, the aforementioned high-temperature ideal-gas limits for $C_{V,\text{ion}}$, P_{ion} , and S_{ion} are still obeyed since the Debye model reduces to the Mie–Grüneisen model at high temperatures.

This Cell model elegantly gives rise to a liquid description similar to the vibration–transit theory proposed by Wallace et al.^{33,34} Using classical MD simulations, Chisolm and Wallace³³ found that the dynamics of a monatomic liquid can be separated into three characteristic temperature domains: (1) at low temperatures, the dense liquid ion behaves almost like a solid ion, with motions controlled by nearly harmonic valleys; (2) at intermediate temperatures, the motion of a liquid ion fluctuates within single valleys and intervalley transitions (transits); (3) at high temperatures, the ionic contribution of a liquid approaches the ideal-gas limit. At low temperatures where $T \leq T^*$, the Cell model assumes that an ion exhibits solid-like behavior. For the high-temperature regime where T

$\gg T^*$, it assumes the liquid ion is a free-moving particle (i.e., an ideal gas) between two repulsive walls. The Cell model smoothly connects these two temperature regimes with a heat capacity that falls from $3 k_B/\text{atom}$ to $3/2 k_B/\text{atom}$ with increasing temperature.

Electron-Thermal Free Energy. Unlike the case of the cold energy or the ion-thermal free energy, we do not use phase-specific models for the electron-thermal free energy $F_{\text{electron}}(T, V)$. Instead, we apply the same F_{electron} model for all three phases. Specifically in the case of L42, we have employed LLNL's Purgatorio code^{26,27} to compute DFT free energies under the averaged-atom-in-jellium framework^{26,27,35} and then use these Purgatorio results to model $F_{\text{electron}}(T, V)$. This Purgatorio model is widely recognized as the best available global treatment for the F_{electron} contribution of the liquid, which becomes significant at high temperatures.

Under the averaged-atom-in-jellium approximation, each atom is treated as a spherically averaged, electrically neutral cell embedded in an electron gas "jellium" with a compensating positive charge background. The Dirac equation is solved numerically with an all-electron DFT method using the local density approximation (LDA), with the density of the electrons surrounding the ion in the neutral cell computed from the resulting Kohn–Sham orbitals. The Fermi–Dirac distribution function is used to describe thermal effects on the occupation of the electronic states at finite temperatures. We model the electron-thermal free energy using the expression $F_{\text{electron}}(T, V) = F_{\text{Purgatorio}}(T, V) - F_{\text{Purgatorio}}(T = 0, V)$. That is, we subtract the Helmholtz energy $F_{\text{Purgatorio}}(T = 0, V)$ predicted by Purgatorio at 0 K from its prediction $F_{\text{Purgatorio}}(T, V)$ at the temperature of interest.

We choose the Purgatorio model because it offers substantial improvements in accuracy over the scalar TF theory,^{22,36,37} the latter of which has been widely used in EOS constructions due to its simplicity. The basic TF model (without additional corrections)²² takes a simple approach in which the electronic density is expressed in terms of a Fermi integral described by an electrostatic potential. This potential depends self-consistently on the density through a Poisson equation.^{22,36,37} This TF model has the practical advantage that once calculations have been performed for hydrogen, results for any other element may be obtained by a simple atomic weight and number scaling on the hydrogen results.^{22,37} However, it suffers from low accuracy in many regimes due to its omission of key quantum and relativistic effects. For instance, a major feature that is absent in TF but can be captured in the Purgatorio model is the existence of a quantized shell structure for the electronic configuration. We will show later that there is a pronounced difference between the two models that can be seen at high temperatures along the principal Hugoniot.

Implicit in our treatment are the assumptions that Purgatorio also provides a reasonable approximation for the solids, and that the differences of F_{electron} attributed to crystal structures or ion motions are relatively minor, which was confirmed previously for Be hcp and bcc by Benedict et al.⁸ It is apparent from Figure 1 that F_{electron} is important only in the high-temperature warm-dense-matter and plasma regimes. Thus, there is little incentive for one to follow a more careful treatment that involves phase-specific solid F_{electron} models since F_{electron} is small at the relatively low-temperature conditions where solids are stable. Nevertheless, we provide validation for our choice by comparing Purgatorio with a phase-specific F_{electron} models from the study by Benedict et al.⁸

To develop their models, Benedict et al. perform *ab initio* calculations of the electronic density of states for each phase, and they fit the results for each phase separately to a low-temperature Sommerfeld expansion. It turns out that Purgatorio and the Benedict et al. structure-specific models predict similar slopes ($\partial P_{\text{electron}}/\partial T$) for the electron-thermal pressure, as shown in Figure 2. They agree with each other far

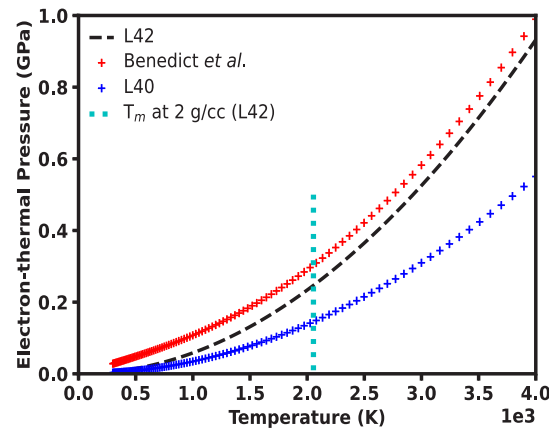


Figure 2. Electron-thermal pressure as a function of temperature along the $2 \text{ g}/\text{cm}^3$ isochore for L42, L40, and phase-specific (this figure covers hcp and liquid) *ab initio*-based electron-thermal models from Benedict et al.⁸

more closely than they do with the TF electron-thermal model used by L40. Not shown in the figure is the curve given by S2024, which is also TF-based and is very similar to L40. The vertical line in Figure 2 indicates the melt temperature of L42 at $2 \text{ g}/\text{cm}^3$. Note that the Benedict et al. F_{electron} models show no significant changes when transitioning from the hcp to the liquid phase. These results confirm that even though Purgatorio ignores the details of crystal structure, it provides a reasonable approximation of the electron-thermal contribution for solid phases.

Numerical Implementation of Purgatorio and Maxwell Construction. Purgatorio. Despite offering improvements over scalar TF theory, the widespread adoption of Purgatorio has been hindered by the fact that the subtraction $F_{\text{Purgatorio}}(T, V) - F_{\text{Purgatorio}}(T = 0, V)$ mentioned above leads to unphysical behavior at low densities and low temperatures. We have developed a practical scheme to clean up this pathological behavior, which enables us to use Purgatorio in the L42 baseline for Be and should be applicable to other materials as well. Figure 3 illustrates the behavior of $F_{\text{electron}}(T, V)$ that we obtain from Purgatorio with and without the cleanup procedure. Below a bounding value T_b of $5 \times 10^4 \text{ K}$, the isotherms predicted by Purgatorio for F_{electron} are clearly unphysical for densities less than a borderline value ρ_b . The T_b and ρ_b represent the upper-bound temperature and density, respectively, of the blue box in Figure 3. Their exact values are material dependent and happen to be $5 \times 10^4 \text{ K}$ and $0.5 \text{ g}/\text{cm}^3$ in the case of Be. There have been many attempts to fix the issues depicted in Figure 3 since Purgatorio's inception over a decade ago.^{26,27} While significant progress has been made, none of these attempts have proven to be fully satisfactory because they tend to also modify the behavior at higher densities, and these modifications have resulted in, for instance, undesired slope changes in the predicted Hugoniot curves. We circumvent this issue by applying the cleanup only at densities

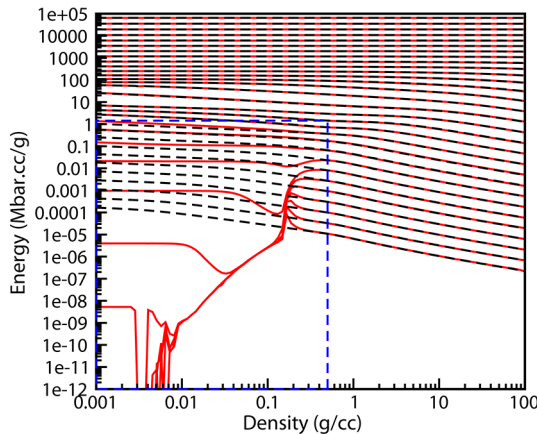


Figure 3. Comparison of the electron-thermal free energy $F_{\text{electron}}(T, V)$ predicted by Purgatorio with and without the pathology cleanup procedure. The curves depict a total of 30 isotherms uniformly spaced from 10^2 – 10^9 K on a logarithmic scale. The blue box encloses the relatively low temperature and density conditions where the cleanup procedure has been applied. The energy along the y-axis is in units of Mbar·cc/g = 100 kJ/g. Although our EOS is applicable to densities as low as 10^{-7} g/cm³ and the blue box extends out to this lower bound, we have restricted the range here for visual clarity.

below ρ_b or volumes above $V_b = m/\rho_b$ (where m is the molar mass) and only for $T < T_b$; we do not apply the cleanup in compression (note that $\rho_b = 0.5$ g/cm³ is lower than the ambient density of 1.85 g/cm³) where the electron-thermal term makes a significant contribution (Figure 1). We recommend the following simple, yet effective, formula for the cleanup:

$$F_{\text{Purgatorio}}^{\text{electron}}(T, V) = F_{\text{Purgatorio}}^{\text{electron}}(T, V_b) \frac{F_{\text{TF}}^{\text{electron}}(T, V)}{F_{\text{TF}}^{\text{electron}}(T, V_b)}$$

$$T < T_b, V > V_b \quad (10)$$

in which $F_{\text{TF}}^{\text{electron}}$ refers to predictions from the scalar TF electron-thermal model. The resulting behavior after cleanup is much more physically reasonable, as demonstrated in Figure 3. We have also verified that $F_{\text{Purgatorio}}^{\text{electron}}(T, V)$ obtained from this procedure obeys conditions required for thermodynamic stability, such as a positive heat capacity.

Maxwell Construction. In multiphase EOS generation, Maxwell construction is used to resolve the stability and thermodynamic boundaries of each phase. For a system in thermodynamic equilibrium, the condition for mechanical stability requires pressure P to increase monotonically with density ρ . Without a Maxwell construction, this requirement may not be met for first-order phase transitions, since there may be occurrences of a van der Waals loop on the pressure–density curves. Thus, Maxwell construction is one of the key operations in any multiphase EOS, and its computational speed is essential for achieving fast EOS construction. From a mathematical standpoint, Maxwell construction is a functional transformation by which a function is replaced by its convex envelope (i.e., the “common tangent rule”). Alternative definitions can be given in terms of its derivatives being forced to be monotonic by the “equal area rule.”³⁸

Over the years, many different Maxwell construction algorithms have been developed. One common approach is based on the total Gibbs energy G , and it involves searching for the conditions such that G is equal for both phases. Another

approach is to find the common tangent between two crossing free-energy–volume curves along an isotherm (Figure 4). The

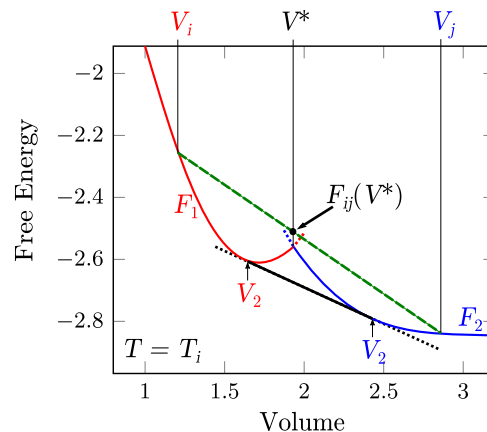


Figure 4. Illustration of the Maxwell construction. Free energies of two phases or models are defined individually (red and blue curves). The resulting Maxwell construction can be seen as a new function in which points with a “common tangent” are joined by a straight line (a portion of the red + blue solid curve is replaced by solid black line). The common tangent portion (solid black line) can be obtained by minimizing the value of $F_{ij}(V^*)$ as explained in the text, in which $F_{ij}(V^*)$ is a linear-interpolated value between energies at points V_i and V_j and is evaluated at the spinodal volume V^* .

slope of the common tangent line represents the phase transformation pressure. Finding the common tangent requires solving nonlinear systems of equations, therefore in the general case the construction almost exclusively requires a numerical treatment. It is for this reason that Maxwell construction is commonly treated separately (i.e., *a posteriori*) from the underlying models.

The new Maxwell construction algorithm we propose falls into the second category described above. It converts the common tangent search into an optimization problem that can be easily parallelized to achieve fast computational speeds. Figure 4 shows two free-energy curves F_1 and F_2 as a function of volume for phases labeled “1” and “2”, at constant temperature. The volumes V_i and V_j are two arbitrary volumes corresponding to F_1 and F_2 , respectively. A single expression for searching the common tangent solutions of V_1 and V_2 is expressed as

$$\min_{ij} \left\{ F_{ij}(V^*) = F(V_i) + \frac{[F(V_j) - F(V_i)](V^* - V_i)}{V_j - V_i} \right\} \quad (11)$$

Minimizing the value of $F_{ij}(V^*)$, at any volume point V^* in the region of interest but in particular for the intersection point (spinodal volume), will give the tangent line between minimizing points V_1 and V_2 .

Note that this formula does not require numerical evaluation of derivatives and root finding. For a given temperature, a naive implementation of this formula is quadratic in the number of tabulated points [$O(n^2)$], with two nested loops: one loop for each of indices i and j , although linearithmic algorithms exist [$O(n \log n)$].^{39–41} A quadratic implementation is sufficient for most practical tables since the number of volume points n is typically only the order of a few hundred. In summary the Maxwell construction is recast as a numerical convexification

Table 1. Our DFT Results for the Cold Curve of the hcp Phase Computed with Different XCFs

ρ (g/cm ³)	Pressure (Mbar)										
	RPBE	revPBE	optB88	PBE	HSE	PW91	PBE0	vdw-DF2	AM05	PBEsol	LDA
2.00	0.113	0.108	0.070	0.077	0.071	0.075	0.069	0.050	0.064	0.058	0.022
2.13	0.216	0.211	0.169	0.177	0.171	0.173	0.169	0.148	0.161	0.158	0.116
2.27	0.347	0.338	0.293	0.300	0.295	0.299	0.293	0.269	0.282	0.278	0.233
2.42	0.503	0.493	0.448	0.452	0.447	0.450	0.445	0.422	0.431	0.426	0.378
2.59	0.696	0.685	0.637	0.640	0.635	0.637	0.632	0.609	0.614	0.613	0.558
2.77	0.933	0.920	0.869	0.871	0.866	0.867	0.864	0.838	0.840	0.840	0.779
2.96	1.221	1.206	1.152	1.153	1.148	1.148	1.145	1.117	1.116	1.112	1.051
3.18	1.573	1.556	1.499	1.498	1.493	1.492	1.489	1.461	1.454	1.451	1.385
3.42	2.005	1.987	1.928	1.922	1.918	1.916	1.915	1.887	1.870	1.868	1.798
3.68	2.535	2.515	2.456	2.444	2.441	2.437	2.437	2.412	2.383	2.382	2.308
3.97	3.185	3.162	3.106	3.086	3.083	3.078	3.079	3.060	3.012	3.013	2.937
4.29	3.985	3.960	3.905	3.876	3.874	3.868	3.870	3.858	3.790	3.794	3.714
4.65	4.975	4.947	4.894	4.855	4.854	4.845	4.851	4.852	4.753	4.758	4.680
5.05	6.212	6.181	6.129	6.078	6.081	6.070	6.077	6.092	5.958	5.967	5.891
5.50	7.769	7.734	7.687	7.623	7.628	7.614	7.623	7.653	7.479	7.493	7.423
5.99	9.755	9.715	9.672	9.595	9.603	9.587	9.597	9.648	9.422	9.442	9.382

Table 2. Our DFT Results for the Cold Curve of the bcc Phase Computed with Different XCFs

ρ (g/cm ³)	Pressure (Mbar)										
	RPBE	revPBE	optB88	PBE	HSE	PW91	PBE0	vdw-DF2	AM05	PBEsol	LDA
2.03	0.124	0.117	0.073	0.085	0.077	0.082	0.075	0.053	0.072	0.070	0.026
2.16	0.229	0.222	0.175	0.187	0.179	0.183	0.177	0.150	0.171	0.169	0.122
2.30	0.359	0.351	0.303	0.313	0.305	0.309	0.303	0.278	0.294	0.293	0.243
2.45	0.520	0.510	0.461	0.469	0.461	0.465	0.458	0.436	0.447	0.446	0.392
2.62	0.715	0.705	0.654	0.660	0.651	0.656	0.649	0.629	0.634	0.632	0.575
2.80	0.954	0.942	0.888	0.893	0.885	0.888	0.882	0.864	0.862	0.856	0.799
3.00	1.249	1.236	1.176	1.181	1.174	1.175	1.170	1.150	1.145	1.138	1.077
3.22	1.610	1.594	1.532	1.535	1.527	1.529	1.524	1.508	1.491	1.485	1.419
3.46	2.049	2.032	1.969	1.967	1.960	1.960	1.956	1.930	1.914	1.909	1.839
3.73	2.585	2.566	2.507	2.495	2.488	2.488	2.484	2.468	2.433	2.430	2.357
4.03	3.246	3.224	3.167	3.147	3.140	3.139	3.138	3.143	3.074	3.072	2.996
4.35	4.063	4.039	3.981	3.955	3.947	3.945	3.944	3.951	3.867	3.867	3.791
4.71	5.081	5.054	4.997	4.962	4.956	4.951	4.952	4.966	4.858	4.860	4.785
5.12	6.354	6.324	6.270	6.223	6.217	6.212	6.214	6.240	6.099	6.106	6.032
5.57	7.957	7.923	7.876	7.814	7.811	7.805	7.807	7.855	7.665	7.678	7.610
6.08	9.991	9.951	9.912	9.842	9.839	9.823	9.834	9.907	9.652	9.674	9.623

(finding the convex envelope) of a set of points describing the free-energy surface. The numerical accuracy is ultimately controlled by the resolution grid in which the free energy $F(V_i)$ is defined.

■ AB INITIO QUANTUM CALCULATIONS

We have performed *ab initio* quantum calculations to supplement experimental data. In particular, the results of these simulations provide new information about Be EOS properties at temperature–density conditions where experimental data are currently not available or not readily accessible with existing laboratory capabilities. We focus on two regions in particular: high-pressure bcc and the high-temperature liquid.

DFT Cold Curves for hcp and bcc. Multiple *ab initio* studies, some dating back four decades ago, have predicted that the α -Be hcp phase transforms to the bcc phase under compression.^{8,9,16,42–45} All of these studies unanimously agree that hcp and bcc are very close in energy, but the theoretically determined transition pressure can differ dramatically because the calculated energy and zero-point motion are extremely

sensitive to computational details. Early theoretical work report low hcp–bcc transition pressures of 2 Mbar or less at 0 K. This contradicts more recent experimental DAC studies, which have not observed any indications of the bcc phase up to 2.05 Mbar at ambient temperature. Later, several *ab initio* investigations revised the predictions to higher pressures up to 4.0 Mbar. Most of these *ab initio* studies use DFT with either the LDA⁴⁶ or PBE XCF.⁴⁷ Given that the DFT-predicted cold pressure is known to be sensitive to the choice of XCF, we have examined the effect of this choice on the Be compression curve as well as its impact on the predicted hcp–bcc transition boundary, which strongly depends on the relative energy between the two phases. Furthermore, we seek to identify which XCF best agrees with experimental static-compression data in order to define constraints for our baseline EOS.

We aim to achieve this by performing 0 K DFT static calculations with 11 different types of XCFs for both the hcp and bcc phases. We use the Be [1s²2s²] PAW pseudopotential (effectively an all-electron description) implemented in the VASP software package. Our simulations employ a 500 eV plane-wave cutoff with Brillouin zone sampling restricted to a

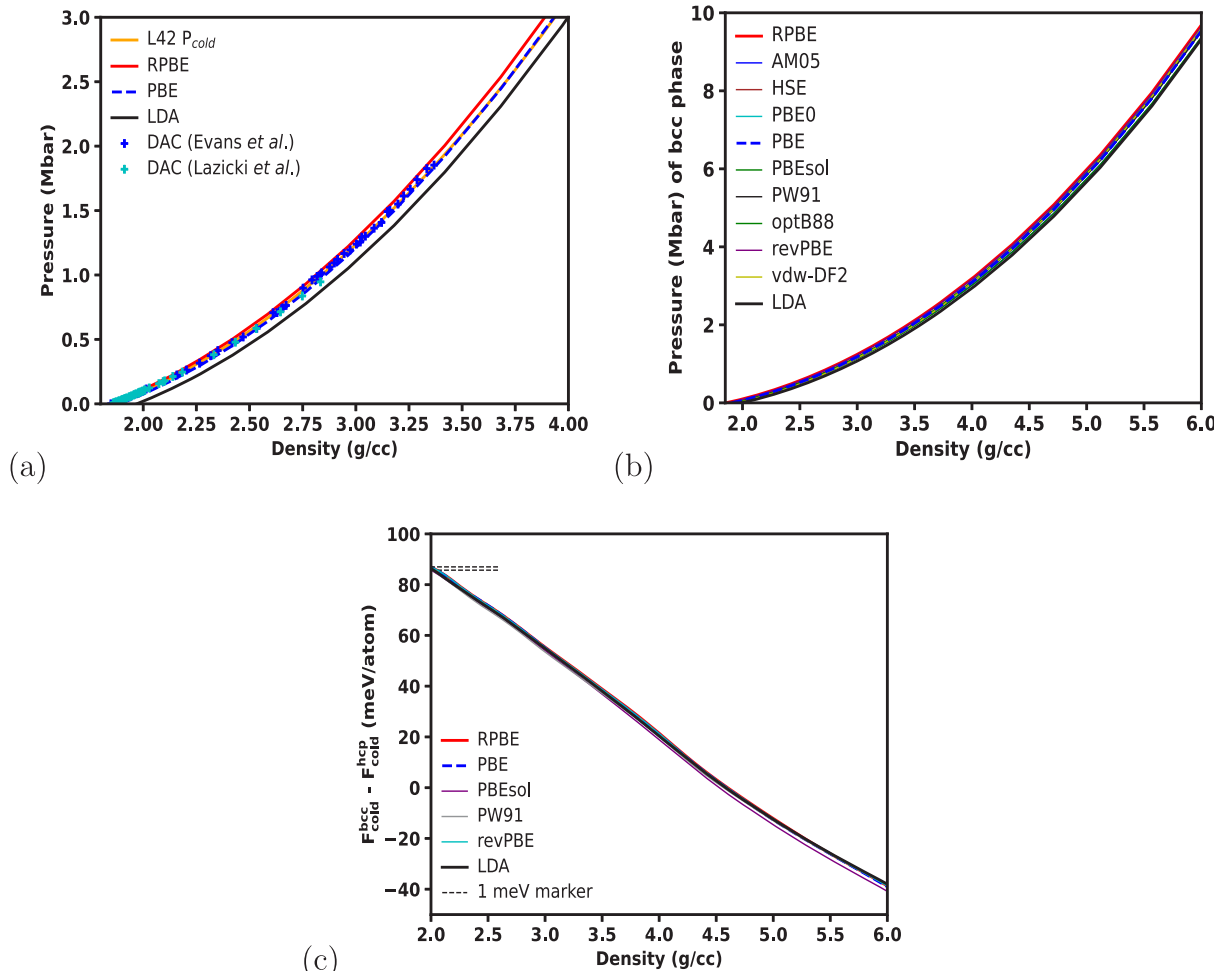


Figure 5. Cold curves of the two solid phases: (a) comparison of the hcp cold curve from our L42 EOS and cold-curve results from a few select XCFS^{46–48} with room-temperature DAC data on the hcp phase;^{19,49} (b) DFT predictions of the bcc cold curve from a set of 11 commonly used XCFS for metals^{46–48,50–59} that we have examined in this study; (c) DFT predictions for the difference $\Delta F_{\text{cold}}^{\text{bcc}} = F_{\text{cold}}^{\text{bcc}} - F_{\text{cold}}^{\text{hcp}}$ in the cold energy between bcc and hcp as a function of density for different XCFS. For clarity, (a) shows results only for the PBE XCF,⁴⁷ which agrees best with the DAC data, and the LDA and RPBE XCFS, which provide lower and upper bounds, respectively, on the cold pressure.

$14 \times 14 \times 14$ Γ -centered k-point Monkhorst–Pack grid,⁶⁰ which we have verified produces results that are converged with respect to a finer $20 \times 20 \times 20$ k-point mesh. Our DFT results are provided in Tables 1 and 2. We compare our results for the hcp phase with existing room-temperature DAC experimental data^{19,49} in Figure 5a. Assuming that the ion-thermal pressure at 300 K is negligible, our results identify PBE⁴⁷ as the XCF that best matches the hcp DAC experiments. Even though PBE near ambient pressures produces a stiffer EOS (a larger pressure for a given density), the agreement improves with increasing pressure. This suggests that among the 11 XCFS illustrated in Figure 5b, PBE would be the most suitable one for the high-pressure bcc phase.

When plotting the DFT-predicted 0 K energy differences $\Delta F_{\text{cold}}^{\text{bcc}-\text{hcp}} = F_{\text{cold}}^{\text{bcc}} - F_{\text{cold}}^{\text{hcp}}$ between hcp and bcc as a function of density, we discovered that the RPBE, PBE, and LDA results almost collapse onto a single curve. Figure 5c shows that $\Delta F_{\text{cold}}^{\text{bcc}-\text{hcp}}$ is remarkably insensitive (<1 meV difference) to the choice of XCF. However, upon examining a wider range of XCFS beyond those shown in Figure 5c, we did encounter larger differences (up to 11 meV) for certain XCFS that are designed to study systems with complexities beyond those found in bulk metals, such as hybrid functionals for chemical

reactions and XCFS designed to model surface interactions and van der Waals forces. The potential impact of these larger $\Delta F_{\text{cold}}^{\text{bcc}-\text{hcp}}$ uncertainties on the hcp–bcc phase boundary will be addressed later through EOS variations. Once we realized that relative quantities (e.g., cold energy) between phases are much less sensitive than absolute quantities, we built free-energy models of the bcc phase in relation to those of the hcp phase. Specifically, we use PBE to compute the energy difference between bcc and hcp along the cold curve and add this difference to our hcp cold curve to produce the bcc cold curve in our EOS.

SQDFT Calculation for High-Temperature Liquid Regimes. High-temperature conditions are extremely important for inertial-confinement fusion applications.⁶¹ However, there are currently no available experimental or theoretical data at these temperatures for Be. Quantum mechanical calculations using traditional DFT methods become prohibitively expensive at such conditions due to the need to compute increasing numbers of partially occupied orbitals (excited states) as the temperature increases. To reach such conditions with full Kohn–Sham accuracy, we therefore employ the newly developed Spectral Quadrature (SQ) method,^{62,63} which is designed specifically for the warm-

dense matter and plasma regimes. It allows us to obtain pressure and energy information on liquid Be at temperatures as high as a few hundreds of electronvolts. Here, we give a brief description of the SQ method, along with some calculational details and results.

The SQ method is a density-matrix-based $O(N)$ method for the solution of the Kohn–Sham equations that is particularly well suited for calculations at high temperature. All quantities of interest, such as energies, forces, and pressures, are expressed as bilinear forms or sums of bilinear forms that are then approximated by quadrature rules that remain spatially localized by exploiting the locality of electronic interactions in real space.⁶⁴ In the absence of truncation, the method becomes mathematically equivalent to the recursion method⁶⁵ with the choice of Gauss quadrature, while for Clenshaw–Curtis quadrature, the Fermi operator expansion⁶⁶ in Chebyshev polynomials is recovered. The method is applicable to metallic and insulating systems alike, with increasing efficiency at higher temperature as the Fermi operator becomes smoother and density matrix becomes more localized.⁶³ $O(N)$ scaling is obtained by exploiting the locality of the density matrix at finite temperature, while the exact diagonalization limit is obtained with increasing quadrature order and localization radius. Convergence to standard $O(N^3)$ planewave results, for metallic and insulating systems alike, is readily obtained.⁶³

In the present work, we employ the massively parallel Spectral Quadrature Density Functional Theory (SQDFT) code⁶⁷ for high-temperature Kohn–Sham calculations of beryllium. SQDFT implements the SQ method in real space using a high-order finite-difference discretization wherein sub-Hamiltonians are computed and applied at each finite-difference grid point. We perform two types of SQDFT calculations: static SQ calculations (SQ-static) and SQ molecular dynamics (SQ-QMD). SQ-static is a computationally less expensive alternative to SQ-QMD, in which the nuclei are kept fixed in a static lattice and the ion-thermal contribution is instead calculated through an *ex post facto* ideal-gas model. SQ-QMD refers to QMD simulations where SQDFT is applied to compute the electronic structure and atomic forces that are used to move the ions about in a classical manner through standard molecular dynamics algorithms. For efficient SQ-QMD simulations, Gaussian quadrature is employed to calculate the density and energy in each self-consistent field iteration whereas Clenshaw–Curtis quadrature is employed for the calculation of atomic forces and pressure.⁶⁸

In all our SQ calculations, we use an all-electron Optimized Norm Conserving Vanderbilt (ONCV)⁶⁹ pseudopotential with cutoff radius of 0.60 au. We also use a finite-difference grid spacing of 0.16 au, Gauss and Clenshaw–Curtis quadrature orders of 28 and 56, and localization radius of 1.3 au in order to obtain pressures converged to 0.4% error or less. Unlike low-temperature conditions, the effect of exchange and correlation for high temperature conditions has been shown to be relatively small. Following previous work on light elements at such conditions,⁷⁰ we model exchange and correlation interactions within the local density approximation.⁷¹ SQ-QMD simulations are carried out in the isokinetic ensemble using a Gaussian thermostat⁷² with ~400 steps for equilibration followed by ~2500 steps for production.

We have performed SQ-static Be calculations on a fcc lattice along four isotherms ranging from 87.1 to 348.3 eV (roughly

$(1.0\text{--}4.0) \times 10^6$ K) over densities spanning 1.850–8.325 g/cm³. In addition, we have performed SQ-QMD simulations along the two lower-temperature isotherms (87.1 and 116.1 eV) covering the same density range as the SQ-static calculations. The resulting SQ-static and SQ-QMD results are listed in Table 3 and illustrated in Figure 6. Notice that

Table 3. Ab Initio Isotherm Pressures and Densities from Both SQ-static and SQ-QMD Calculations

<i>T</i> (eV)	ρ (g/cm ³)	P (Mbar)	
		SQ-static	SQ-QMD
87.1	1.850	69.37	70.24 ± 0.28
	3.700	134.26	136.52 ± 0.55
	5.550	198.69	202.38 ± 0.81
	7.400	263.42	268.66 ± 1.07
	8.325	296.16	303.25 ± 1.21
	116.1	98.84	100.04 ± 0.40
	3.700	191.83	194.37 ± 0.78
	5.550	283.42	287.85 ± 1.15
	7.400	374.61	381.15 ± 1.52
	8.325	420.38	428.05 ± 1.71
174.2	1.850	157.51	
	3.700	308.34	
	5.550	456.72	
	7.400	603.89	
	8.325	677.30	
	348.3	331.51	
	3.700	656.43	
	5.550	978.35	
	7.400	1299.23	
	8.325	1458.15	

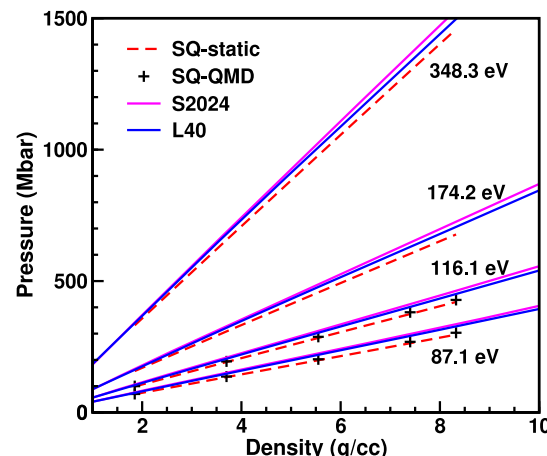


Figure 6. Comparison of predictions from the SQDFT code⁶⁷ and two existing EOSs (L40⁵ and S2024⁷) along four high-temperature isotherms. SQ-QMD results are presented only for the two lower temperatures; the agreement with SQ-static at these two temperatures is already quite good and would be expected to improve further with increasing temperature.

results from the two types of SQ calculations agree rather well with each other for the two isotherms depicted in the figure, and their agreement is expected to improve further at even higher temperatures as the ideal-gas model in SQ-static provides an increasingly better approximation of the nuclei motion in SQ-QMD. This suggests that SQ-static is a reliable

alternative to SQ-QMD for the high-temperature regimes where the ion-thermal contribution is nearly ideal-gas-like.

At temperatures above tens of electronvolts, like those shown in Figure 6, the electron-thermal free energy is the leading contributor to the total Helmholtz free energy F . The figure shows that L40⁵ and S2024⁷ both overpredict the pressure. The main reason is that the electron-thermal models of both EOSs are based on TF theory,^{22,36,37} which results in overionization and an excess electron pressure at certain conditions. The Baseline section explains how we have developed our L42 EOS so that it achieves better agreement with SQDFT predictions. As it turns out, this requires using not only Purgatorio instead of TF but also a more accurate ion-thermal model.

L42 BASELINE RESULTS AND DISCUSSION

In this section, we first present important details on how we have constructed the L42 baseline EOS, including constraints and fitting of model parameters. We then illustrate the performance of our EOS by comparing it against various sets of experimental data and theoretical predictions.

EOS Constraints, Model Parameters, and Phase Diagram. There are a total of nine free-energy terms that must be determined among the hcp, bcc, and liquid phases. We approximate the F_{electron} contribution of the three phases with the Purgatorio model as described in the Methodology section. This simplification leaves us with a total of six free-energy terms, with two terms per phase— F_{cold} and F_{ion} —that need to be resolved.

For each phase, we have used an assortment of EOS constraints to calibrate the cold energy F_{cold} and ion-thermal free-energy F_{ion} models. Figure 7 shows the (ρ, T) locations for key constraints that we considered when building these models. For some measurements, either the density or the temperature is unavailable. In these cases, we estimate the missing ρ or T information using our EOS (e.g., to calculate Hugoniot temperatures). The solid segments of the full-range melt and Hugoniot curves represent the approximate (ρ, T) ranges of the published melt and Hugoniot data. The stability fields of the individual phases are labeled to indicate the types of constraints that are available for each phase. Notice that the majority of constraints pertain to hcp. Our DFT cold-curve calculations partly make up for the complete absence of experimental data for the bcc phase, while our new SQDFT results provide much-needed information about the high-temperature liquid, a regime that has otherwise been completely neglected in past studies. Additional theoretical constraints used, but not displayed, in Figure 7 are *ab initio* PDOS calculations reported by Benedict et al.⁸ for both the hcp and bcc phases.

Besides accounting for the existing EOS constraints, our EOS must also obey fundamental asymptotic limits. For example, at sufficiently low densities (e.g., $\rho \leq 10^{-3}$) the EOS must converge to the ideal-gas limit (green vertical box in Figure 7). This limiting condition requires that (1) the cold energy approaches a constant (i.e., becomes independent of density) whose value is set by the cohesive energy and (2) the Grüneisen parameter γ approaches 2/3. At extremely high temperatures (e.g., the orange horizontal box in the figure), Be is a fully ionized plasma with an ion-thermal heat capacity that (neglecting relativistic effects) converges to the high-temperature limit of $7.5 k_B/\text{atom}$, where each of the 4 electrons plus the nucleus contributes $3/2 k_B/\text{particle}$ due to their transla-

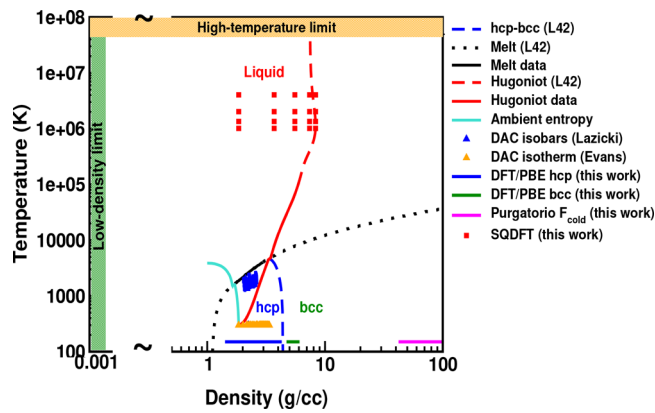


Figure 7. Density–temperature locations (some are estimates) for key EOS constraints used in the development of L42. The density axis is plotted on a logarithmic scale with \sim symbolizing continuation to the lower density of 10^{-3} g/cm^3 . The hcp–bcc transition boundary, the full-range principal Hugoniot, and the melt curve predicted by L42 are shown as dashed or dotted curves. Existing melt and Hugoniot data sets are included as two solid segments of the full-range curves. Our DFT calculations with the PBE XCF for the hcp and bcc cold curves, as well as the Purgatorio cold curve at high densities, are also added for comparison. (Although these cold curves are calculated at 0 K, they are displayed in this figure at a low, but nonzero temperature of 150 K because the temperature axis is on a logarithmic scale.) The green vertical box at the left edge and orange horizontal box at the top indicate the (ρ, T) regimes that are expected to approach the low-density ideal gas and fully ionized plasma limits, respectively. In addition, we also have the one-component plasma limit at extremely high densities that lie beyond those shown in the figure.

tional modes. On the extreme-compression side, we approximate the cold curve with predictions from Purgatorio.^{26,27} (In theory, the Purgatorio cold curve reaches the Thomas–Fermi limit as V approaches zero, though perhaps surprisingly we have observed that this convergence does not yet occur even at densities as high as 10^3 g/cm^3 .) The limiting value of the Grüneisen parameter γ at extreme compressions is 1/2.⁷³ A crucial point that we emphasize is that these physics-based limitations are explicitly built into the free-energy forms that we use in this work. Our overall goal in developing the EOS is to therefore produce free-energy models that reproduce known high-fidelity physics data in the relatively narrow range of conditions where they are available (Figure 7), and provide a reasonable interpolation to connect these regions to the correct asymptotic limits.

The determination of the F_{cold} and F_{ion} models for the hcp phase is entirely based on experimental data. Specifically, the cold curve of hcp is optimized against experimental DAC room-temperature (roughly 300 K) isotherms.^{19,49} (Strictly speaking, this determination also depends on the choice of the thermal model, but in practice the thermal pressure P_{ion} at 300 K is not significant compared to the cold pressure P_{cold} .) The hcp ion-thermal contribution, which is described by the Debye model in eq 4, is largely based on two sets of measurements: (1) ambient-pressure entropy data⁷⁴ and (2) recent DAC isobars.¹⁹ The two key quantities for the ion-thermal model are the Grüneisen parameter $\gamma(V)$, which is constrained heavily by information pertaining to thermal pressures (e.g., DAC isobars), and the associated reference Debye temperature $\theta_{\text{ref}} = \theta(\rho_{\text{ref}})$, which is fit to ambient-pressure entropy data.⁷⁴ Once these two quantities are determined, the Debye temperature θ

Table 4. Fitting Parameters from Different Studies for the Cold Curve of Each of the Three Phases^a

phase		ρ_0 (g/cm ³)	E_0 (meV/atom)	B_0 (GPa)	B'_0
hcp	this work (L42)	1.853	0.0	111.3	3.67
	Benedict et al. ⁸	1.930	0.0	113.2 (300 K)	3.66 (300 K)
	Lazicki et al. ¹⁹	1.841		111.5	3.69
	Evans et al. ¹⁸			104.58 (300 K) 114 (300 K) 109.88 (300 K)	3.63 (300 K) 3.27 (300 K) 3.59 (300 K)
bcc	this work (L42)	1.872	78.2	113.6	3.64
	Benedict et al.	1.964	108	116.7	3.64
liquid	this work (L42)	1.756	135.2	95.6	3.62
	Benedict et al.	1.882	149	112	3.64

^aThe DAC studies by Evans et al.¹⁸ and Lazicki et al.¹⁹ are conducted at room temperature (300 K), while we list the values of the bulk modulus B_0 and its pressure derivative B'_0 from L42 and those reported by Benedict et al.⁸ at both 0 and 300 K, the latter of which are labeled. The L42 isotherms reported here are fits over a limited density range from 1.7–4.0 g/cm³ with the Vinet–Rose form in eq 2.

Table 5. Fitting Parameters for the Grüneisen Parameter γ as a Function of V and the Debye temperature $\theta_{\text{ref}} = \theta(\rho_{\text{ref}})$ at a Selected Reference Density ρ_{ref} for the Three Phases in L42^a

phase	ρ_{ref} (g/cm ³)	θ_{ref} (K)	a_0	a_1	a_2	a_3
hcp	1.85	948	0.3805	0.1085	0	0
bcc	1.93	890	0.4778	0.07845	-0.01095	0.003655
liquid	1.83	663	1.029	-0.8559	0.3538	-0.03527

^aHere, γ is fit to a polynomial of the form $\gamma = a_0 + a_1 V + a_2 V^2 + a_3 V^3$ in the following ranges: 3.87 Å³/atom ≤ V ≤ 7.49 Å³/atom (between 3.87 and 2.00 g/cm³) for hcp, 1.0 Å³/atom ≤ V ≤ 5.0 Å³/atom (between 15.0 and 3.0 g/cm³) for bcc, and 3.0 Å³/atom ≤ V ≤ 5.0 Å³/atom (between 5.0 and 3.0 g/cm³) for liquid. The units of the polynomial coefficients are such that γ is dimensionless when V is in units of Å³/atom.

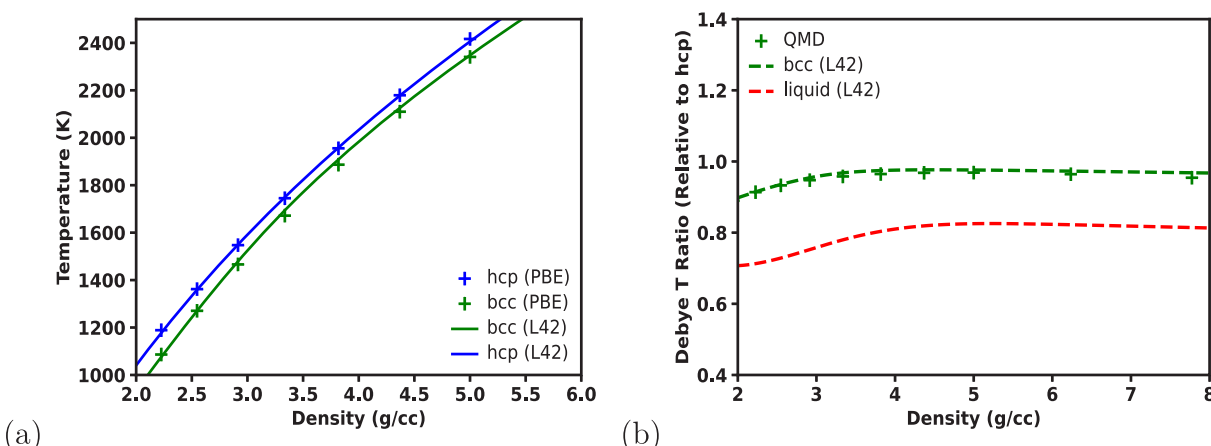


Figure 8. (a) Debye temperatures of bcc and hcp of L42 plotted alongside Debye temperatures reported by Benedict et al.,⁸ which they have inferred from PDOS calculations obtained via QMD simulations with the PBE functional. (b) Ratio of the Debye temperature of bcc and liquid to that of hcp in our EOS plotted alongside the bcc-to-hcp Debye temperature ratio ($\theta^{\text{bcc}}/\theta^{\text{hcp}}$) reported by Benedict et al.

= $\theta(V)$, which is the only adjustable parameter that appears in the Debye model (4), is completely determined through the relation $\gamma = -d \ln \theta / d \ln V$. As a consistency check, we will show later that the resulting hcp EOS agrees well with experimental data on the Hugoniot, which depend on both cold and ion-thermal models.

In order to make comparisons to models reported in the literature, we have fit the cold curve and ion-thermal model of hcp to analytical functions over a limited density range. Table 4 lists the parameters of the Vinet–Rose fit for the cold curve, and Table 5 contains parameters for $\gamma(V)$, as well as the corresponding θ_{ref} and ρ_{ref} values. Notice that our 300 K bulk modulus of 113.2 GPa is slightly higher than our 0 K value of 111.3 GPa, and it is designed to fall between the DAC-reported values of 109.88 GPa (Evans et al.¹⁸) and 114 GPa (Lazicki et al.¹⁹). Our value for the bulk modulus B_0 and its

pressure derivative B'_0 at 0 K are similar to those reported by Benedict et al., but the value of the initial density ρ_0 , where the cold energy is at its minimum, is rather different. Their value of 1.93 g/cm³ is noticeably larger than the ρ_0 of 1.853 g/cm³ in L42. This is understandable, given that the cold curve in Benedict et al.⁸ is based on DFT calculations with the PBE XCF,⁴⁷ which is known to have difficulties in reproducing the experimental ambient density.

We now continue with a description of the construction of the EOS for the bcc phase in L42. Unlike the situation for hcp where there is a relative abundance of experimental data, there are no such data for bcc. Thus, our approach with bcc has been largely guided by theory. We use *ab initio* theoretical predictions to calculate differences between bcc and hcp and use these differences and the already developed hcp EOS to obtain the free-energy models for the bcc phase. In particular,

the bcc cold curve $F_{\text{cold}}^{\text{bcc}}$ and its Debye temperature $\theta^{\text{bcc}}(V)$ are obtained in the following manner:

$$F_{\text{cold}}^{\text{bcc}}(\rho) = F_{\text{cold}}^{\text{hcp}}(\rho) + \Delta F_{\text{cold}}^{\text{bcc}-\text{hcp}}(\rho) + \Delta F_{\text{ZPE}}^{\text{bcc}-\text{hcp}} \quad (12)$$

$$\theta^{\text{bcc}}(V) = \theta^{\text{hcp}}(V) \frac{\theta_{\text{PDOS}}^{\text{bcc}}(V)}{\theta_{\text{PDOS}}^{\text{hcp}}(V)} f_{\text{mod}}(V) \quad (13)$$

where $\Delta F_{\text{cold}}^{\text{bcc}-\text{hcp}}$ and $\Delta F_{\text{ZPE}}^{\text{bcc}-\text{hcp}}$ are energy differences between the two solid phases attributed to the DFT/PBE-derived results listed earlier and zero-point energy, respectively. In addition, $\theta(V)^{\text{bcc}}_{\text{PDOS}}$ and $\theta(V)^{\text{hcp}}_{\text{PDOS}}$ are the Debye temperatures derived from PDOS calculations with the PBE functional as reported by Benedict et al.,⁸ while $f_{\text{mod}}(V)$ is a modulation function that we tune to obtain the desired outcome, including the placement of the hcp–bcc boundary and the hcp–bcc–liquid triple point. It turns out that the PDOS/PBE calculations from Benedict et al. provide a good ansatz so that we only need to make small adjustments to their results [i.e., $f_{\text{mod}}(V) \approx 1$ over a wide range of volumes]; see Figures 8a,b. We may again fit the resulting bcc cold curve and the ion-thermal models over a narrow range of densities with the same analytical functions as in the case of hcp; the corresponding parameters are listed in Tables 4 and 5. The main differences between the L42 bcc model and that of Benedict et al. concern the values of E_0 and ρ_0 in the cold curve. For example, L42 has an E_0 of 78.2 meV, which is about 30 meV lower than the value reported by Benedict et al. This may be due to differences in accounting of the zero-point energy since L42 includes this term in the cold energy, while Benedict et al. do not.

The construction of a multiphase EOS is an iterative process, requiring numerous rounds of refinement and a consideration of a multitude of different constraints. This is particularly true for the liquid phase. We cannot isolate the cold energy of this phase experimentally since the liquid is not the stable phase at low temperatures. Therefore $F_{\text{cold}}^{\text{liquid}}$ is a purely theoretical construct that serves as a temperature-independent free-energy term. We have explored the possibility of obtaining an estimate of the cold pressure by performing 0 K DFT calculations on a set of liquid configurations annealed from QMD simulations. Unfortunately, the computed energy averaged over an ensemble of configurations is too scattered to be useful for EOS construction. Thus the cold and ion-thermal models of this phase must be developed simultaneously through an iterative, largely trial-and-error process until good agreement is achieved for the chosen constraints.

The available data and theory for constraining the liquid EOS include (1) ambient-pressure liquid entropy data reported by National Institutes of Technology (NIST),⁷⁴ (2) reported liquid data along the Hugoniot, and (3) our SQDFT high-temperature liquid isotherms. In addition, the phase boundary between the solids and liquid (melt curve) are extremely sensitive to the relative energy differences between phases. Thus they are critical in guiding the overall multiphase construction since they couple the free energies of different phases together. The aforementioned liquid constraints are used to simultaneously optimize its cold and ion-thermal models. The resulting models may be fitted to the same analytic functions chosen for hcp and bcc, with parameters listed in Tables 4 and 5. The obtained ρ_0 value of 1.756 g/cm^3 for our liquid cold curve is less than that of 1.882 g/cm^3 reported by Benedict et al.⁸ With this liquid model, we are also

able to reproduce reported properties of the melt curve at ambient pressure, namely the melt temperature of 1560 K ⁷⁴ and liquid density of 1.695 g/cm^3 . Similar to many other materials, our liquid phase has a noticeably smaller bulk modulus B_0 than the solid phases. With all three phases of our L42 EOS having now been constructed, Figure 9 shows the temperature and density conditions where each of the three phases are predicted to be thermodynamically stable.

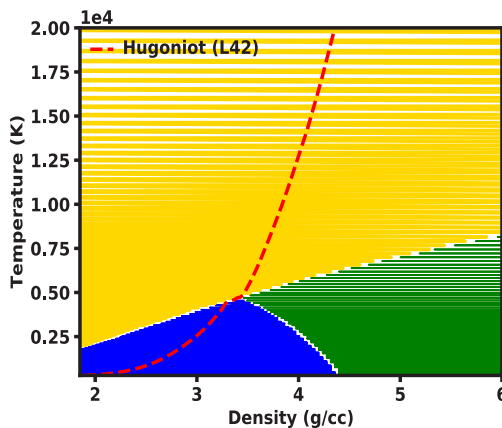


Figure 9. Temperature–density phase diagram predicted by L42, where the hcp, bcc, and liquid phases are colored in blue, green, and gold, respectively. Two-phase regions are colored in white, while the dashed curve shows the predicted principal Hugoniot.

So far we have focused primarily on EOS construction in a limited density range since these intermediate densities are of greatest interest to most studies on Be. It nevertheless represents only a small portion of the global range (10^{-7} – 10^3 g/cm^3) over which we intend our EOS to be applicable. Data throughout most of this range is scarce, as evident in Figure 7. Our cold-curve construction is therefore centered around ensuring that it approaches the correct theoretical limits at the two extreme density ends and provides a reasonable interpolation to connect the intermediate density regime with these limits. At the low-density end, which we refer to as the expansion region, we have designed the cold curve so that it approaches the ideal-gas limit. An important part of satisfying this limit is to adjust the cold curve so that it reproduces the reported value of 3.32 eV ³² for the cohesive energy, which represents the energy difference between the hcp phase at ambient conditions and an ideal gas of vaporized Be atoms (see Figure 10a). Another property of interest on the expansion region is the critical temperature, which L42 predicts to be about 6500 K , a reasonable approximation to the reported theoretical value of 5205 K .⁷⁵ Fortunately, the fact that the EOS of the expansion region is not well constrained for most materials is usually not a concern for hydrodynamic simulations of ICF (and many other high-pressure applications) since in simulations of such phenomena, EOS predictions in this region are often overridden by other constitutive models, such as damage or liquid-cavitation models. Nevertheless, we are currently working on an improved scheme for the critical temperature and density and, more generally, the EOS in the expansion region. At high compressions ($\rho > 40 \text{ g/cm}^3$), we fit the cold curve of the liquid and solid (bcc) to predictions from Purgatorio, which provides a good description of highly dense states. The fit to

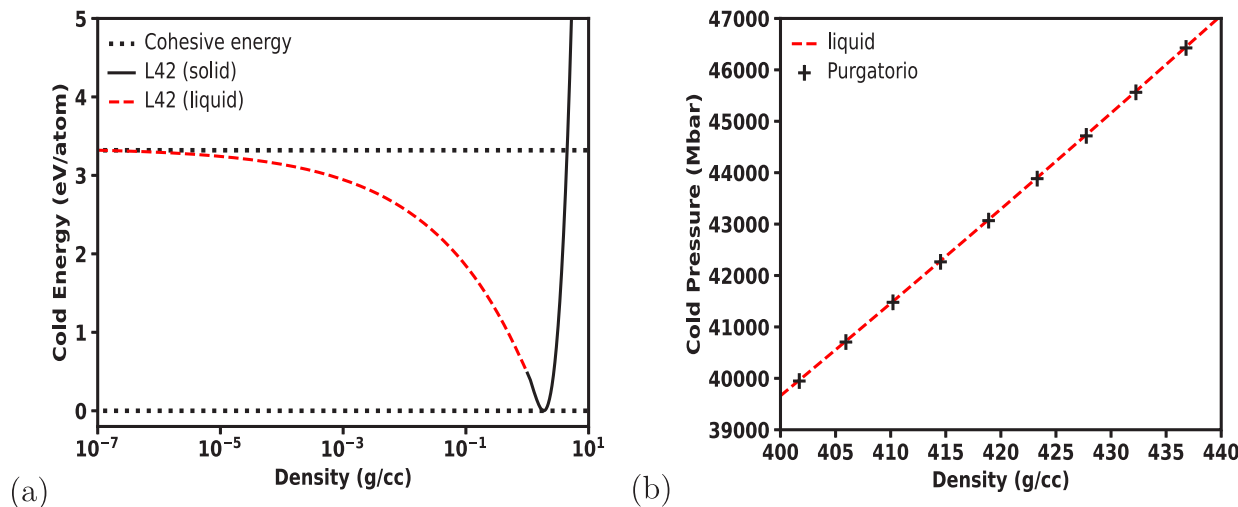


Figure 10. Cold energy as a function of density for two limiting cases: (a) the expansion region where the two horizontal dotted lines indicate the reported cohesive energy of 3.32 eV;³² (b) the extreme-compression side constrained by the computed Purgatorio cold curve.

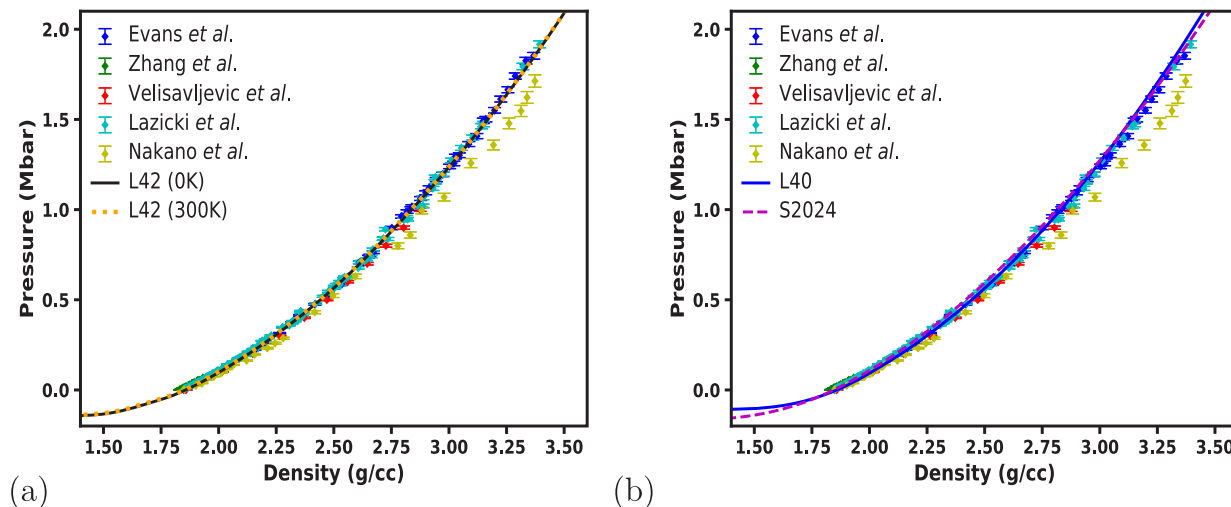


Figure 11. Room-temperature isotherm of the hcp phase from different Be EOSs compared against experimental static-compression (e.g., DAC) results^{19,49,70,76,77} on this phase: (a) L42; (b) L40 and S2024.

the Purgatorio cold curve at extreme pressures in the liquid is illustrated in Figure 10b.

Comparison with Experimental and Theoretical Data.

DAC isotherms. We first illustrate our models for the hcp cold energy, which are fit to DAC studies on the room-temperature isotherm. The thermal pressure at 300 K is negligibly small, which is why the 0 K isotherm and 300 K isotherm from L42 sit on top of each other, as indicated in Figure 11. It is possible to anchor the EOS to only a subset of the experimental work because there is a large scatter in the reported measurements. Part of this scatter is because Be has a poor X-ray scattering efficiency and therefore produces weak X-ray diffraction patterns, due to its low atomic number Z. Experimental discrepancies may also be attributed to differences in the choice of pressure media (or the absence of a medium) and the choice of pressure standard. For instance, as shown in Figure 11, data from Nakano et al.⁷⁷ are by far the softest (i.e., they suggest the greatest compressibility for the isotherm) and are extremely scattered. Their work was conducted without any pressure medium and also employed an older ruby pressure scale. In addition, we note that their reported isotherm is

noticeably more compressible than that obtained from DFT calculations performed with the LDA functional,⁴⁶ the latter of which is considered to provide an upper bound on the compressibility. Evans et al.⁴⁹ have used helium and argon pressure media in order to reduce nonhydrostatic effects. At higher pressure, their isotherm is slightly stiffer than that from a later study published by Lazicki et al.,¹⁹ which uses helium and sodium chloride pressure media along with a different pressure standard. However, the trend is reversed at lower pressures where the isotherm from Lazicki et al. becomes stiffer than that from Evans et al. By adjusting our cold energy to an average of these two studies (Table 4), we are able to obtain a good fit to the room-temperature isotherm throughout the entirety of the range in Figure 11a. In comparison, a careful examination of Figure 11b reveals that L40 agrees fairly well with experiments at lower pressures but becomes slightly too stiff at higher pressures, while the opposite is true for S2024.

DAC Isobars and Ambient-Pressure Entropy Data. Next we proceed to compare EOS performances against an assortment of isobar data. An important subset of these data pertain to isobar measurements obtained from DAC studies,

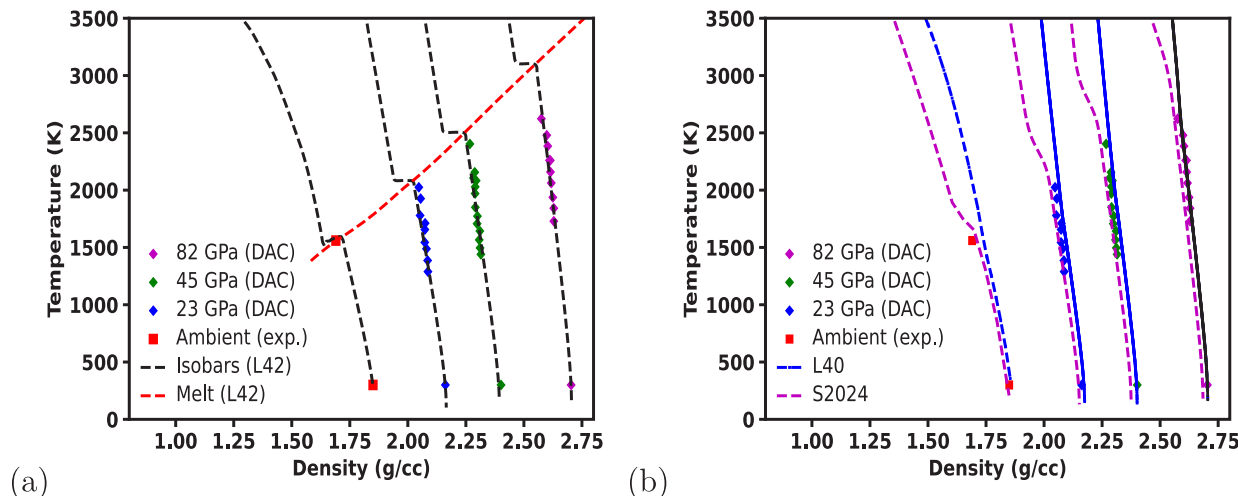


Figure 12. Comparison between EOS predictions on isobars in the hcp and liquid phases and experimental results: (a) L42 compared against hcp-phase data taken from DAC measurements performed by Lazicki et al.;¹⁹ (b) L40 and S2024 compared against Lazicki et al.

which are shown in Figure 12. The isobar data displayed in this figure are consistent with the room-temperature isotherm data portrayed earlier in Figure 11. When compared to the isobar data, our L42 baseline EOS performs rather well, as shown in Figure 12a. In contrast, L40 is too soft at lower pressures but gets progressively stiffer at higher pressures, while the opposite is true for S2024 (Figure 12b). Another important type of isobar information is the ambient-pressure entropy data taken from the online NIST database.⁷⁴ As shown in Figure 13, our

Hugoniot. The principal Hugoniot, which illustrates material properties under compression by a steady, shock wave, represents a rich source of data to constrain our EOS, as there have been many studies conducted on this thermodynamic curve. A significant portion (>2.05 Mbar) of the principal Hugoniot resides in the liquid phase (Figure 14a). A couple of studies have performed high-pressure, nuclear-impedance-matching (NIM) experiments to shock compress Be into liquid states that are partially ionized. Ragan⁸⁰ and Nellis et al.⁷⁹ have conducted separate experiments with that technique to achieve pressures as high as 10 and 17 Mbar, respectively. The data collected from these two experiments have no direct overlap, but taken together they suggest a noticeable deviation in the Hugoniot curvature $dP/d\rho$, with Ragan's data being softer than those from Nellis et al. A likely reason for this discrepancy is that Ragan and Nellis et al. use different EOS standards to analyze their data. A later study by Knudson⁸⁶ concludes that the aluminum standard used by Nellis et al. is inaccurate. This prompted Kerley⁶ to reanalyze the Nellis et al. data with an improved aluminum standard, which yields results that are more consistent with Ragan's work (using a molybdenum standard). Although all three EOSs depicted in Figure 14a fall within the error bars of the NIM data, L40 and S2024 may overestimate the pressure since their predictions just barely pass through the error bars of Ragan, while the L42 Hugoniot falls closer through the center of the uncertainty range.

Figure 14b shows that L42 is able to closely reproduce hcp-phase Hugoniot data at pressures below 1 Mbar. Above this pressure, there is a noticeable scatter in the reported data, as the results from Isbell et al.⁸³ suggest much softer behavior than those reported by the more recent study by McCoy et al.⁷⁸ Since the latter was published more than 50 years after the former, and many diagnostic and theoretical advancements have occurred over the course of this period, we are more inclined to believe McCoy et al.⁷⁸ Nevertheless, L42 predicts a Hugoniot that falls within the error bars of both studies and agrees with the QMD-predicted sound speeds from McCoy et al. (Figure 14c). If we were to make our Hugoniot stiffer so that it falls closer to the middle of the experimental uncertainty range in McCoy et al., we would not obtain good agreement with their own QMD predictions and with the experimental

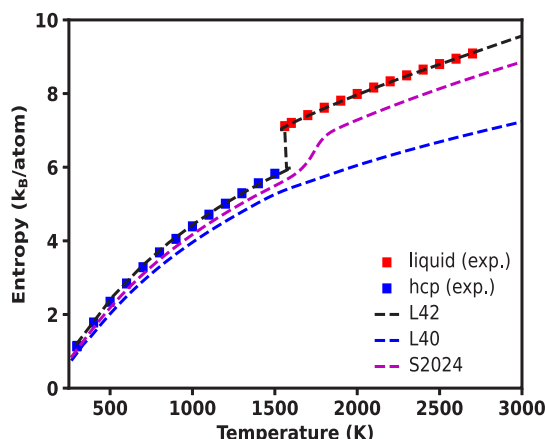


Figure 13. Comparison of experimental data and predictions from three different EOSs (L42, L40, S2024) on the ambient-pressure entropy for the hcp and liquid phases. The experimental data are taken from an online NIST database.⁷⁴

EOS models for hcp and the liquid phase closely reproduce these NIST data. In contrast, both L40 and S2024 underpredict the entropy of these phases. L40 is not a multiphase EOS, and thus it does not exhibit an entropy change upon melting ΔS_m . Moreover, S2024 appears to overestimate the ambient melt temperature slightly. Note that according to the experimental measurements, Be has an ambient-pressure ΔS_m of $1.47 k_B/\text{atom}$. This value is considerably larger than the $0.87 k_B/\text{atom}$ assumed by Benedict et al., which is based on the standard, rule-of-thumb value of $0.8 k_B/\text{atom}$ for a typical metal.³³

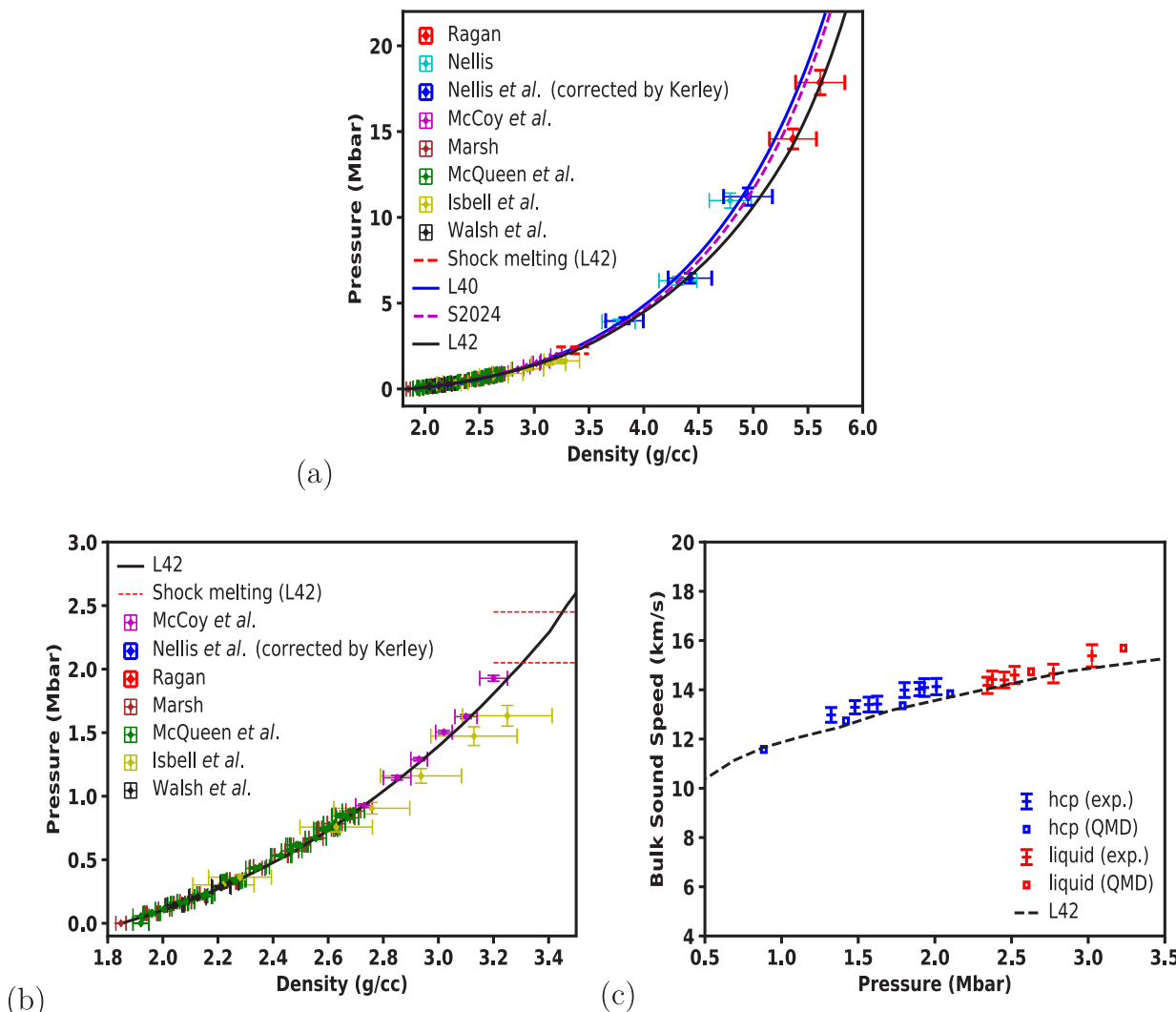


Figure 14. Comparison of experimental data^{6,78–84} and predictions from three different EOSs (L42, L40, and S2024) on the principal Hugoniot: (a) overall view of the entire range covered by the published data, including conditions above the shock-melting pressure of 2.05 Mbar⁷⁸ that extend well into the liquid stability field; (b) hcp-phase results in terms of pressure vs density; (c) the bulk thermodynamic sound speed of hcp plotted alongside experimental and QMD simulation results reported by McCoy et al.⁷⁸ We note that this figure does not include results from Cauble et al.,⁸⁵ who report Hugoniot results derived from high-intensity laser experiments at pressures as high as 15 Mbar. Unfortunately, their data exhibit large uncertainties that are greater than 20%, which is more than double the uncertainty of the high-pressure Ragan⁸⁰ and Nellis et al.⁷⁹ experiments and are not reliable enough to use as an EOS constraint.

isobars in Figure 12(a) since all of our curves in that figure would get shifted to the left in that event.

Phase Diagrams and Shock-Melting Behavior. The search for the elusive high-pressure bcc phase and the hcp–bcc–liquid triple point have inspired decades of experimental and theoretical studies. Relatively recent *ab initio* investigations have predicted hcp–bcc transition pressures as high as 4 Mbar.^{9,16,87} These higher-pressure conditions are difficult to examine in conventional DAC experiments and may require utilization of the new toroidal DAC technique.⁸⁸ However, since the hcp–bcc phase boundary has a negative slope ($dT/dP < 0$), the transition pressure is expected to decrease with increasing temperature. For instance, Robert et al.⁹ suggest in their multiphase EOS study that the hcp–bcc–liquid triple point occurs at ~ 0.95 Mbar and ~ 3500 K, which are conditions that are well within reach of conventional DAC experiments. To confirm this prediction, Lazicki et al.¹⁹ incorporated X-ray diffraction and laser heating in DAC experiments to search for the bcc phase over an extensive range

of temperatures up to 4000 K and pressures up to 2.05 Mbar, but they report observing only the hcp solid. Their DAC results provide a lower bound for the hcp–bcc transition pressure and indicate that the triple point suggested by Robert et al. is too low (Figure 15). The higher triple point of ~ 1.8 Mbar and ~ 4300 K predicted by Benedict et al.⁸ is likely to be more accurate. However, further adjustment of the hcp–bcc–liquid triple point toward an even higher pressure (e.g., 2.25 Mbar) is needed in order achieve better consistency with both the DAC results¹⁹ and the observations of the recent dynamic shock-melting study of Be.⁷⁸

Dynamic-compression experiments have led to the same conclusions regarding the stability of bcc. X-ray patterns of Be shock compressed to 1.82 Mbar at Sandia's Z pulsed-power facility⁸⁶ found evidence only of the hcp phase, and not the bcc phase. More recently, McCoy et al.⁷⁸ conducted magnetically accelerated flyer-plate experiments at the Z facility to measure the bulk (c_b) and longitudinal (c_l) sound velocities along the shock Hugoniot using a well-established overtaking rarefaction

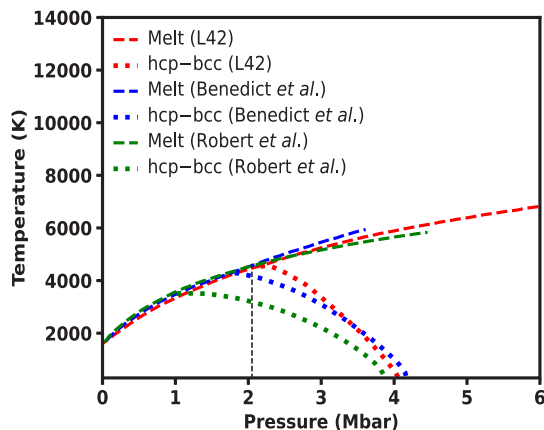


Figure 15. Comparison of the bcc stability field and the hcp–bcc–liquid triple point in three different EOSs: L42, Robert et al.,⁹ and Benedict et al.⁸ The last two are often-cited EOSs regarding the triple point. The dashed vertical line indicates the lower-bound value of 2.05 Mbar for the hcp–bcc transition pressure suggested by static-¹⁹ and dynamic-compression^{78,86} experiments. In order to be consistent with those experiments, the triple point must lie to the right of this line.

technique. They use the disappearance of shear waves to identify the onset of melting, thus making theirs the first experimental determination of the shock melting pressure of Be. Their value of 2.05 Mbar is noticeably higher than the 1.65 Mbar prediction made by Robert et al.⁹ but is closer to the 1.95 Mbar value predicted by Benedict et al.⁸ McCoy et al. also tried to identify the hcp–bcc transition along the Hugoniot. Given the similarities between bcc and hcp, c_b for both phases were found to be nearly identical, though c_l does exhibit a small, but measurable separation between bcc and hcp. Since the measured c_l along the Hugoniot undergoes a smooth and gradual decay toward melting, McCoy et al. conclude that there is no hcp–bcc phase transition prior to shock melting. This agrees with the static-compression results of Lazicki et al. since both studies imply a lower-bound hcp–bcc transition pressure of 2.05 Mbar. Figure 15 shows that we have developed our EOS to be consistent with these experimental observations. We have done this largely by adjusting the volume dependence of the Debye temperature $\theta^{bcc}(V)$ of the bcc phase through the modulation function $f_{mod}(V)$ in eq 13.

At the same time, the determination of $\theta^{bcc}(V)$ also allows us to calculate zero-point energy differences $\Delta F_{ZPE}^{bcc-hcp}$ between bcc and hcp and thereby compute the bcc cold curve according to eq 12.

Turning our attention now to the melt curve, we examine Figure 16a, which shows phase boundaries predicted by L42 plotted against a representative set of reported experimental and theoretical data. The DAC data (blue and red squares) are taken from Lazicki et al.¹⁹ and show that hcp has a remarkably wide range of stability for temperatures up to 4000 K and pressures up to 2 Mbar. Fast recrystallization (red squares) refers to the rapid appearance and disappearance of X-ray diffraction spots observed in their experiments and is considered to be an indication of either partial melting or near melting (i.e., may be interpreted as a lower bound on the melt curve). Notice that our L42 melt curve sits almost entirely above the identified fast recrystallization zone. To pinpoint the shock-melting pressure, we overlay our melt curve and principal Hugoniot on the same plot. The L42 shock-melting pressure is determined to be 2.05 Mbar, which is the same value obtained by McCoy et al.⁷⁸ We note that the temperatures are unknown for their experiments, so to indicate plausible error bars on the actual temperature, we have represented the McCoy et al. shock-melting pressure point as a vertical bar in Figure 16a. Furthermore, the L42-predicted melt curve is consistent with the ambient melt temperature (triangles) from NIST⁷⁴ and the QMD prediction of the bcc phase (black cross) reported by Benedict et al.⁸ The solid branch of the L42 Hugoniot resides entirely in the hcp stability field (does not pass into the bcc region), which is consistent with the fact that McCoy et al. do not report observing bcc in their shock-compression experiments. The hcp–bcc–liquid triple point is predicted by L42 to be approximately 2.25 Mbar, which is slightly higher than the shock-melting pressure.

A similar comparison is performed in Figure 16b for L40⁵ and S2024.⁷ L40 contains a single solid phase that smoothly merges into the fluid phase across a Lindemann-based melt curve. As a result, it does not include a bcc region. As shown in Figure 16b, the L40 melt curve coincides with the onset of rapid crystallization identified by DAC as the lower bound of melt. However, it does underestimate the shock melting pressure by ~0.4 Mbar, which suggests that the L40 melt curve

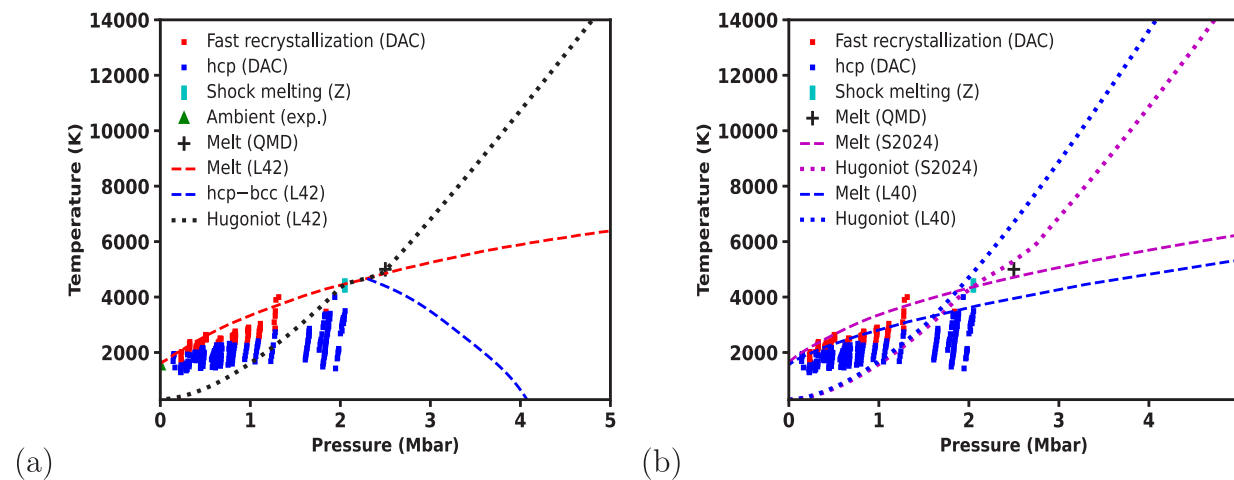


Figure 16. Predictions from different Be EOSs compared against results reported in the literature: (a) phase boundaries (melt and hcp–bcc) and principal Hugoniot results from our L42 baseline; (b) melt curve and principal Hugoniot results from L40⁵ and S2024.⁷

is likely to be too low. In contrast, S2024 is a true multiphase EOS, though there is a lack of reported information regarding EOS construction and the hcp–bcc boundary. The shock-melting pressure of S2024 is 2.01 Mbar, which agrees well with the onset of shock melting observed at 2.05 Mbar by McCoy et al.⁷⁸ despite having been developed a decade before that experimental data was published. This is consistent with the fact that S2024 agrees well with the experimental Hugoniot for hcp solid.

Ab Initio Predictions at High Temperatures. In order to validate the performance of the L42 baseline EOS for the liquid phase at extreme temperatures and pressures, we revisit our SQDFT results presented in the *Ab Initio* section. We compare Figures 6 and 17 and find that our Purgatorio-based

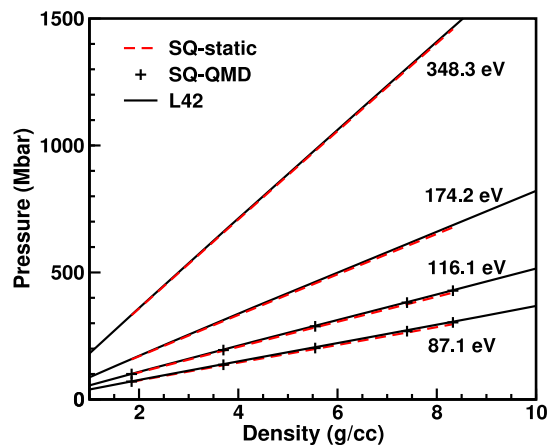


Figure 17. Same as in Figure 6, except that here we now compare SQDFT predictions for high-temperature isotherms of the liquid with those from L42.

L42 baseline agrees noticeably better with the SQDFT calculations than the TF-based L40 and S2024 EOSs. This is because L42 implements models that better approximate the ion-thermal and electron-thermal contributions. Specifically, L42 uses the Cell model^{24,25} in eq 9 for the ion-thermal contribution, which correctly reaches the ideal-gas limit at sufficiently high temperatures. In contrast, L40 uses the Cowan model²² for the ion-thermal contribution, which has a heat capacity that converges more slowly to the ideal-gas limit with respect to temperature, resulting in worse agreement with SQDFT results. We will demonstrate this more clearly in the Variations section, where we present results for the L9422 EOS, which is a Cowan-based alternative to L42 that we have developed.

■ EOS VARIATIONS RESULTS AND DISCUSSION

Overview. We have developed eight EOS variations on our L42 baseline to address different types of uncertainties or constraints, as summarized in Table 6. The table shows that we have considered four categories of variations to address the following issues: (1) ambiguities in the choice of free-energy models, (2) uncertainties imposed by different theoretical treatments, (3) experimental uncertainties, and (4) lack of data in certain conditions. In the first category, we have explored the consequences of changing some of the free-energy models in L42 to “legacy” models, such as those employed by the older QEoS/XEOS formalism. Since many previous global EOSs have relied on TF^{22,37} instead of Purgatorio, mainly due to its

Table 6. Summary of the Eight EOS Variations on Our L42 Baseline

EOS	variation type	variation details
L9421	electron-thermal model	replace Purgatorio with TF
L9422	ion-thermal model	replace liquid Cell model with Debye + Cowan
L9423	theory constraint	decrease $F_{\text{cold}}^{\text{bcc}} - F_{\text{cold}}^{\text{hcp}}$ by −5.75 meV/atom (lower bound suggested by XCFs)
L9424	theory constraint	increase $F_{\text{cold}}^{\text{bcc}} - F_{\text{cold}}^{\text{hcp}}$ by +5.75 meV/atom (upper bound suggested by XCFs)
L9425	experimental data	stiffer Hugoniot
L9426	experimental data	softer compression curve
L9427	lack of information	lower melt temperatures for $P > 3$ Mbar
L9428	lack of information	higher melt temperatures for $P > 3$ Mbar

simplicity and smoothness, we have produced a variation, which we refer to as L9421, that uses the former so that we may directly compare differences in the two models for the electron-thermal free energy. In another variation (L9422), we use a combination of the Debye model and the Cowan model^{22,23} instead of the more recent Cell model^{24,25} to describe the ion-thermal free energy of the liquid. In the second category, we have investigated uncertainties on the bcc cold curve (and hence also the stability of that phase) that arise due to the choice of XCF in DFT calculations. We have examined numerous different XCFs, which together suggest a maximum range of 11.5 meV/atom in the energy difference $\Delta F_{\text{cold}}^{\text{bcc}-\text{hcp}}$ between the DFT-predicted 0 K energies of bcc and hcp, with the PBE XCF we have used in the L42 baseline lying near the middle of this range. Therefore L9423 and L9424 explore the consequences of placing the energy difference at the lower and upper bounds, respectively, of this 11.5 meV/atom range. L9425 and L9426 fall into the third category of accounting for experimental uncertainties, with the former focusing specifically on the Hugoniot in Figure 14, while the latter focuses on the compressibility along the room-temperature isotherm in Figure 11. Finally, L9427 and L9428 are variations where we have changed the melt curve at relatively high pressures where there is a complete absence of data on that particular property. Of course, there are many more variations that one could develop than what we present here, but together these eight variations provide a representative sampling of the ambiguities/uncertainties often encountered during the construction of an EOS, and they illustrate how one could potentially address these uncertainties.

Variations on the Electron-Thermal (L9421) and Liquid Ion-Thermal (L9422) Models. L9421: Variation on the Electron-Thermal Model. In L9421, we have swapped out Purgatorio for TF in modeling the electron-thermal free energy $F_{\text{electron}}(T, V)$ of all three phases. Although less accurate, TF results are much easier to obtain and do not have the pathological behavior that Purgatorio has in certain regimes (see Figure 3). As a result, TF theory has traditionally been used instead of Purgatorio for developing global EOSs. Switching Purgatorio with TF overestimates the pressure along certain conditions, such as the isotherms examined in Figure 18. This is perhaps expected from our discussion of Figures 6 and 17, which show that the TF-based L40 and S2024 EOSs also overpredict the pressure along these isotherms. It is interesting to note, however, that TF does not overestimate the pressure along all thermodynamic paths. For instance, it predicts softer behavior in the lower-pressure

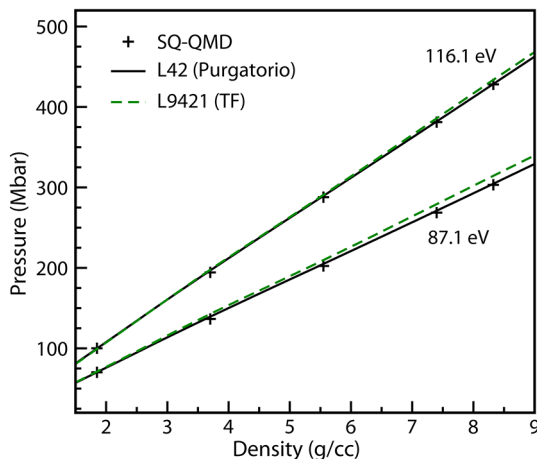


Figure 18. Comparison of our EOS variation L9421 (which has a TF-based electron-thermal model) with the L42 baseline and SQ-QMD calculations along two liquid isotherms.

regime of the principal Hugoniot where experimental data are available (Figure 19a). The overionization tendency of TF results in an excess electron pressure for a given temperature, which is the cause of the stiffer behavior in Figure 18, but this also may result in an overestimation of the heat capacity. Therefore, the temperature of the shocked states are lower in L9421 than they are in L42, leading to a softer Hugoniot.

With increasing temperature, L42 and L9421 are expected to agree better with each other on the basis of the argument that the electrons become more and more free-electron-like. However, this is no longer true at sufficiently high temperatures where relativistic effects, which are neglected in our version of TF theory but are treated explicitly in Purgatorio (and therefore also in L42), become prominent. As depicted in Figure 19b, the two electron-thermal models display a pronounced difference along the principal Hugoniot above approximately 16000 Mbar, beyond which they approach two different compression limits. Above this threshold pressure, the agreement between the two models deteriorates. The TF-based L9421 Hugoniot approaches the scalar asymptotic density limit⁷³ of $4\rho_0$ (7.4 g/cm³ for Be, where $\rho_0 = 1.85$ g/cm³ is the starting density for this Hugoniot). In contrast, L42

achieves a higher density of 8.19 g/cm³ at $T = 10^9$ K ≈ 86 keV, but it is still short of reaching the relativistic asymptotic density limit⁷³ of $7\rho_0$, which may be achieved at extreme temperatures (e.g., $T > 100$ keV) beyond the scope of our EOS.

L9422: Variation on the Liquid Ion-Thermal Model. In L9422, we have replaced the Cell model for the ion-thermal free energy of the liquid with a combination of the Debye model at relatively low temperatures and the Cowan model^{22,23} (used by the QEoS/XEOS methodology) at higher temperatures. The temperature T_{trans} where this Debye-to-Cowan transition occurs depends on the volume V through a Lindemann⁸⁹ expression where

$$T_{\text{trans}}(V) = \alpha V^{2/3} [\theta^{\text{liquid}}(V)]^2 \quad (14)$$

There is no clear-cut way to determine the precise location of this transition curve and, so perhaps as a reasonable placement, we set the value of the constant α so that T_{trans} at ρ_0 is equal to about 90% of the ambient boiling temperature. Although we have changed the functional form of our free-energy models, we leave the Debye temperature—and hence also the Grüneisen parameter—in L9422 unchanged from L42 so that $\theta_{\text{L9422}}^{\text{liquid}}(V) = \theta_{\text{L42}}^{\text{liquid}}(V)$ and $\gamma_{\text{L9422}}^{\text{liquid}}(V) = \gamma_{\text{L42}}^{\text{liquid}}(V)$. As a result, the melt curve $T_m = T_m(V)$ in these two EOSs are virtually the same since the Cell model in eq 9 reduces to the Debye model at relatively low temperatures where $T = T_m \ll T^*$. The transition curve in eq 14 lies above the melt curve. Thus in L9422, we can think of the temperature regime between the melt curve $T_m(V)$ and the transition curve $T_{\text{trans}}(V)$ as an intermediate zone described by a Debye model for a dense liquid. The Debye-to-Cowan transition is apparent in Figure 20a,c. Let us define dimensionless variables $u = \theta/T$ and $w = T_{\text{trans}}/T$. Below the transition curve (i.e., for conditions where $w > 1$), $F_{\text{ion}}^{\text{liquid}}(T, V)$ in L9422 is given by the Debye model F^{Debye} in eq 3. Above the transition curve ($w < 1$), we employ the Cowan model,^{22,23} which yields the following expression for the Helmholtz energy on a per-atom basis:

$$F^{\text{Cowan}}(V, T) = k_B T f(u, w) \quad (15)$$

where the dimensionless function f is defined as

$$f = -\frac{11}{2} + \frac{9}{2}w^{1/3} + \frac{3}{2}\ln\left(\frac{u^2}{w}\right) \quad (16)$$

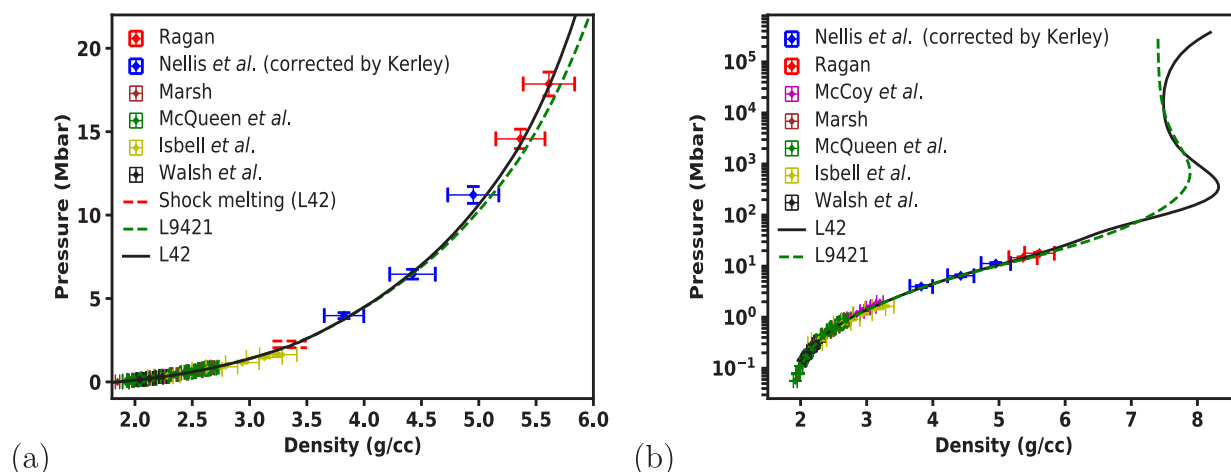


Figure 19. Comparison of L9421 with L42 along the principal Hugoniot illustrated over two different sets of conditions: (a) lower-pressure range^{6,78–84} where experimental data^{6,78–84} reside; (b) global range with the pressure axis plotted on a logarithmic scale.

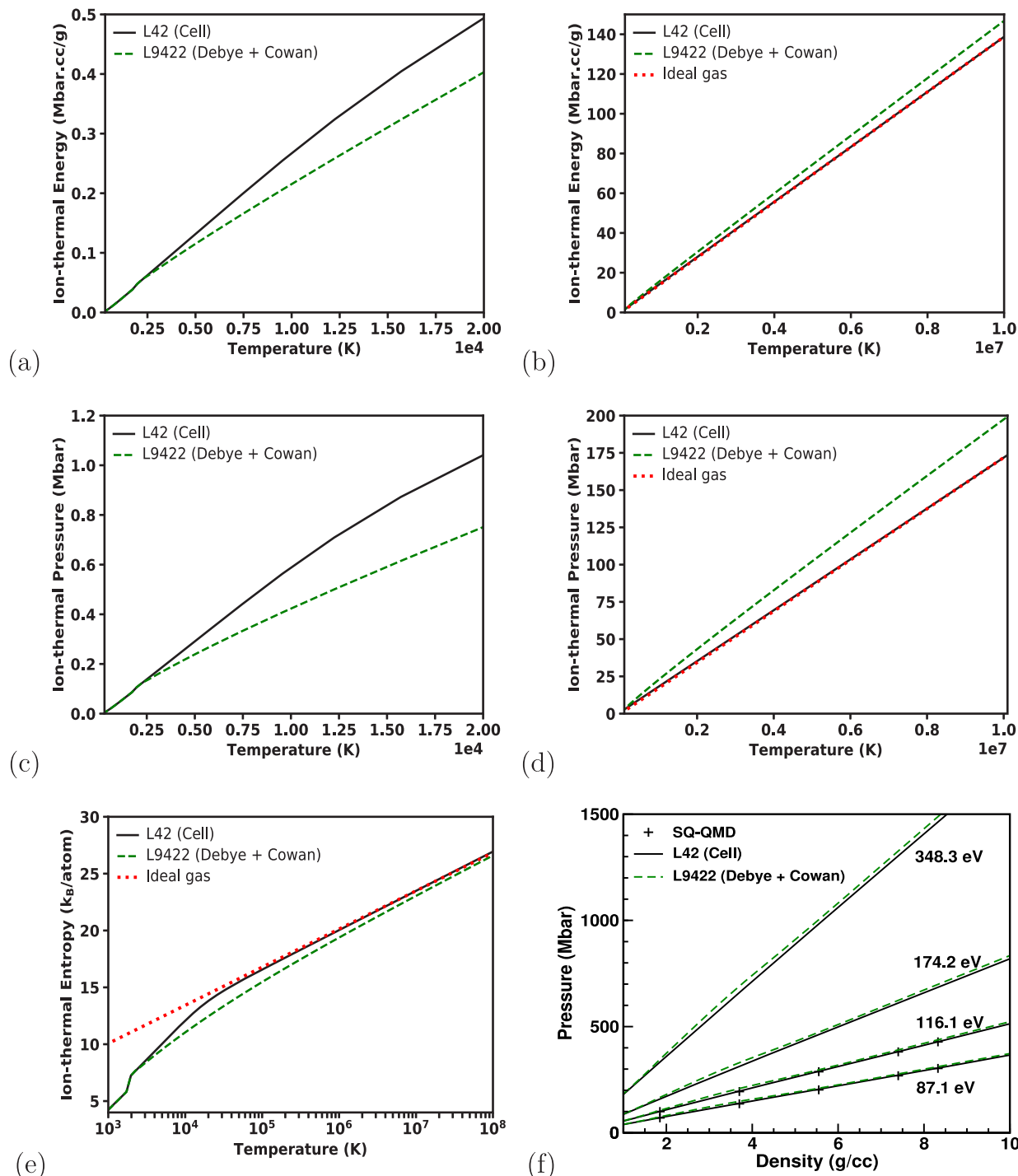


Figure 20. Comparison of different ion-thermal properties of L9422 (which describes the liquid ion-thermal free energy with a Debye + Cowan model) and L42 along the 1.85 g/cm³ isochore: (a) internal energy for $T < 20000$ K; (b) internal energy for $10^5 < T < 10^7$ K; (c) pressure for $T < 20000$ K; (d) pressure for $10^5 < T < 10^7$ K; (e) entropy for $10^3 < T < 10^8$ K on a logarithmic axis. In (f), we illustrate the total pressure predicted by the two EOSs and the SQDFT code⁶⁷ along four high-temperature isotherms. We have also plotted the results of the ideal-gas model in (b), (d), and (e) to show the required limiting behavior at high temperatures.

Along the transition curve where $w = 1$, we have $F^{\text{Debye}} = F^{\text{Cowan}}$, and there is a smooth, continuous transition in other thermodynamic properties as well.

Due to its simplicity, the Cowan model has been used to generate the majority of LLNL EOSs through the QEoS/XEOS methodologies. It provides a reasonable approximation to the ion-thermal behavior of a liquid at high temperatures because, just like the Cell model, it approaches the appropriate

heat-capacity limit of an ideal gas at high temperatures, although Cowan does so at a different rate. The ion-thermal heat capacity $C_{V,\text{ion}}$ in the Cowan description asymptotes at high temperatures to the ideal-gas value of $3/2 k_B/\text{atom}$ in a $T^{-1/3}$ manner,²⁵ instead of the quadratic T^{-2} behavior displayed by the Cell model in eq 7. However, unlike the Cell model, the Cowan model does not go to the desired ideal-gas energy, pressure, and entropy limits (see Figure 20b,d,e).

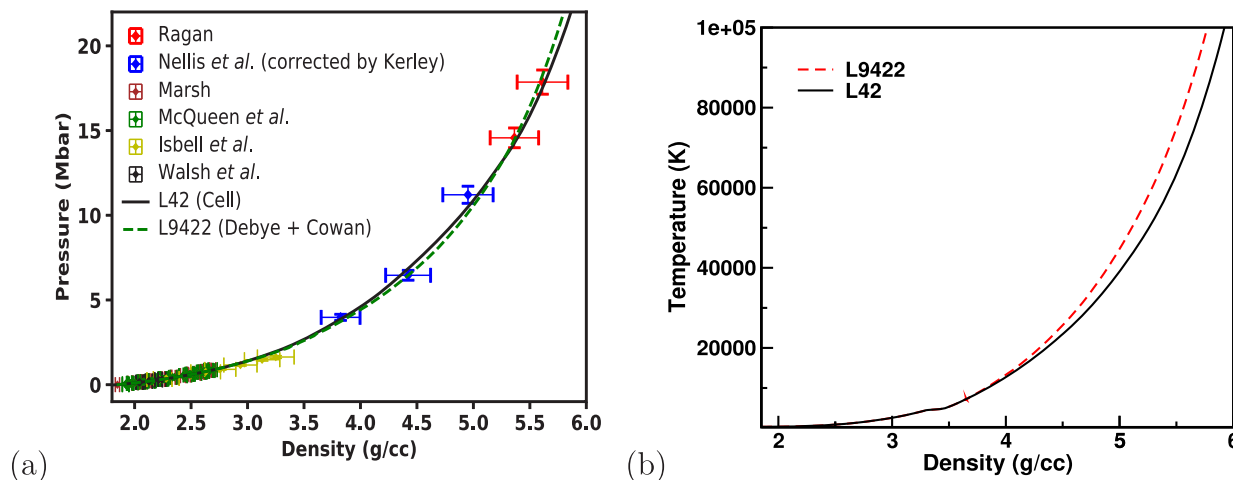


Figure 21. Principal Hugoniot of L9422 and L42 in terms of (a) pressure vs density and (b) temperature vs density. Data from various experimental studies^{6,78–84} are included in (a) for comparison.

As a result, L9422 at these high temperatures does not agree well with L42 or the SQDFT results (Figure 20f). Since the liquid phase in L9422 and L42 are described by the same $\theta(V)$ and $\gamma(V)$, the Hugoniots in $P-\rho$ space obtained from these two EOSs are rather similar as shown by Figure 21a. In contrast, as for the Hugoniot in $T-\rho$ space, the Cowan model at the temperatures illustrated in Figure 21b yields noticeably hotter shocked states than does the Cell model. This is due to their heat capacities being quite different in this temperature range. The increasing disparity in the Hugoniot temperatures explains why L9422 becomes progressively stiffer (though not by much since the Grüneisen parameter γ remains unchanged) compared to L42 with increasing density along the Hugoniot, as shown in Figure 21a.

Theory-Constraint Variations on the bcc Stability (L9423 and L9424). In our earlier discussion of Figure 5 for the L42 baseline, we have reasoned that given the near absence of experimental data on the bcc phase, it is justifiable to use PBE as the XCF of choice to compute the cold curve of that phase in our L42 baseline. We have found that the LDA⁴⁶ and RPBE⁴⁸ XCFs provide plausible lower and upper bounds, respectively, on the bcc (as well as hcp) cold energy. Furthermore, Figure 5c shows that, perhaps surprisingly, all three functionals—as well as a few other commonly used XCFs^{50–52}—predict very similar differences in the cold energy between bcc and hcp, with all of them agreeing to within about 1 meV/atom for $\Delta F_{\text{cold}}^{\text{bcc}-\text{hcp}}$. Recall that this energy difference is added to the experimentally calibrated hcp cold curve to produce the bcc cold curve. Figure 22 shows that if we consider other XCFs beyond those considered in Figure 5c (we have tried a total of 11 XCFs in this study), a few of them^{53–59} do exhibit large differences from each other, with this difference being as large as about 11.5 meV/atom. Therefore, reasonable lower and upper bounds on $\Delta F_{\text{cold}}^{\text{bcc}-\text{hcp}}$ suggested by theory are ∓ 5.75 meV/atom. These bounds lead to the EOS variations L9423 and L9424, respectively.

Adjusting the cold energy of bcc in the manner we have just described has a noticeable effect on the stability of the bcc phase and, thus, also on the hcp–bcc–liquid triple point (Figure 23). As expected, the decreased cold energy of bcc in L9423 compared to L42 expands the stability field of that phase so that the bcc–liquid portion of the melt curve gets shifted to higher temperatures, and the hcp–bcc boundary gets

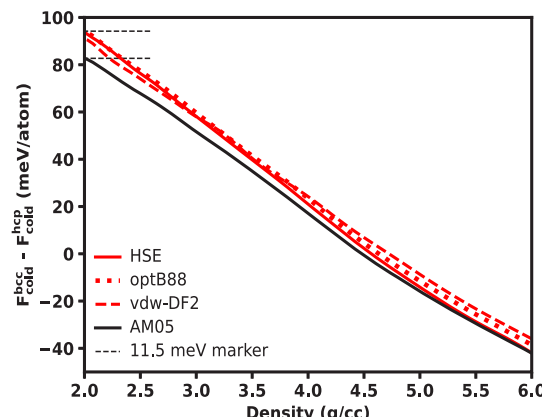


Figure 22. DFT predictions with various XCFs of the energy difference $\Delta F_{\text{cold}}^{\text{bcc}-\text{hcp}}$ between bcc and hcp along the cold curve. Compared to the XCFs shown in Figure 5c, the ones illustrated here^{53–59} display relatively large differences in $\Delta F_{\text{cold}}^{\text{bcc}-\text{hcp}}$ and are designed to deal with complicated phenomena not typically encountered in the study of bulk metals, like chemical reactions and strong surface interactions.

shifted to lower pressures. The opposite is true in L9424, which has a higher-energy and less-stable bcc phase. Phase boundaries are sensitive to even small adjustments in energy. Figure 24 demonstrates that, in contrast, other thermodynamic properties are far more insensitive. The principal isentrope and Hugoniot are essentially unchanged in L9423 and L9424 compared to the L42 baseline. Even though the isentrope is dominated by the contribution from the cold curve, the ∓ 5.75 meV/atom adjustments in the cold energy are very small compared to the magnitude of the change in energy along the isentrope itself.

Experimental-Constraint Variations on the Hugoniot (L9425) and Cold Curve (L9426). L9425: Variation on the Hugoniot. Our discussion of the liquid, high-pressure portion of the principal Hugoniot in Figure 14 noted that the Ragan⁸⁰ and Nellis et al.⁷⁹ studies may perhaps be somewhat inconsistent with each other in the sense that the Hugoniot must undergo a change in curvature in order to pass through the middle of the uncertainty range of both data sets. Our L42 baseline is chosen to fall within the middle of the range of the Ragan data. However, it may be reasonable to construct an

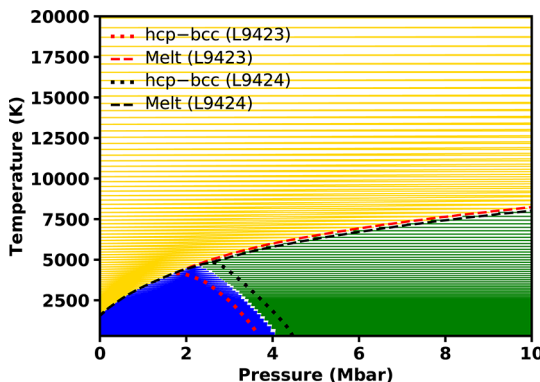


Figure 23. The hcp–bcc (dotted curves) and melt (dashed curves) phase boundaries of our L9423 and L9424 EOSs superimposed on the temperature–pressure phase diagram of L42, in which the hcp, bcc, and liquid phases are colored in blue, green, and gold, respectively. The decrease (L9423) or increase (L9424) of the bcc cold energy affects the stability of that phase and therefore shifts its boundaries with the other phases, most notably the hcp–bcc boundary.

EOS whose Hugoniot passes through the middle of the range in Nellis et al. instead. We have designed L9425 to do exactly that. This EOS is a variation on L42 in which we have multiplied the Debye temperature θ of the liquid by a constant value of 1.123 for densities higher than 3 g/cm^3 , as demonstrated in Figure 25. No change is made for lower densities because we intend to alter the behavior in only the liquid, high-pressure portion of the Hugoniot. However, in order to keep the phase boundaries in L9425 the same as in L42 (so that we can, to the extent possible, focus on modifications to the Hugoniot only), we have performed the same adjustments on θ of the solid phases so that the ratio of the Debye temperatures between different phases remains unchanged. The larger Debye temperature translates to a larger Grüneisen parameter $\gamma = -d \ln \theta / d \ln V$. Figure 26a shows that, as intended, this yields a stiffer Hugoniot that passes through the middle of the range in Nellis et al. In addition, the larger θ and γ result in a stiffer behavior along other

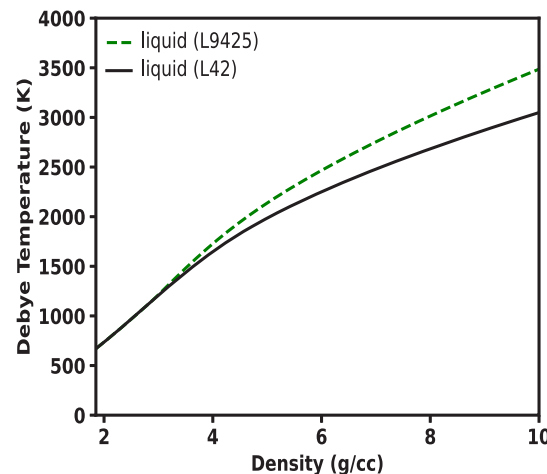


Figure 25. Liquid-phase Debye temperatures of L42 and L9425, in which the Debye temperature of the liquid in the latter EOS is elevated (multiplied by a constant value of 1.123 at densities above 3 g/cm^3) to stiffen the Hugoniot at high pressures.

thermodynamic paths as well, such as the high-temperature isotherms portrayed in Figure 26b.

L9426: Variation on the Cold Curve. L9426 is like L9425 in that both EOSs are constructed to address experimental uncertainties. Specifically, L9426 explores uncertainties in the compressibility of the hcp phase. We have seen from Figure 11 that there is a fair amount of experimental scatter in the hcp room-temperature isotherm. In L9426, we have tuned the cold energy of that phase to fit the data from Velisavljevic et al.,⁷⁶ which yields the softer isotherm depicted in Figure 27a. This in turn results in a softer principal isentrope (Figure 27b) since the behavior along that path is controlled mainly by the cold contribution to the free energy. Panels c and d of Figure 27 show that adjustments to the cold curves do not have a significant effect on the Hugoniot or along high-temperature isotherms since the behavior along these thermodynamic paths are dominated by the ion-thermal and electron-thermal contributions instead.

Variations Due to Lack of Data on the High-Pressure Melt Curve (L9427 and L9428). We have seen earlier that

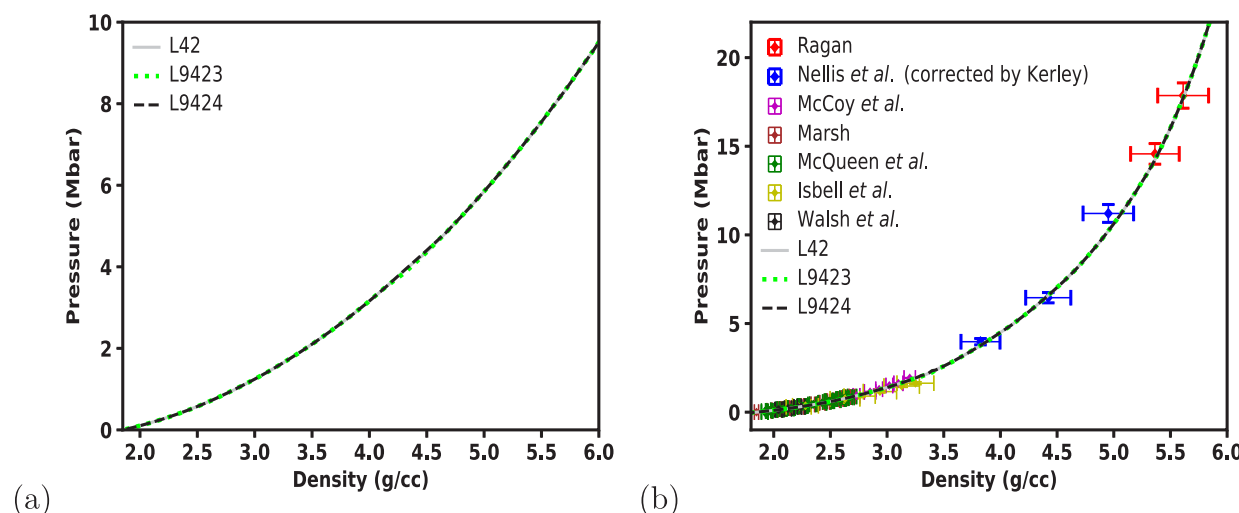


Figure 24. Comparison of L9423 and L9424 with L42 on (a) the principal isentrope pressure vs density and (b) principal Hugoniot pressure vs density. Data from various experimental studies^{6,78–84} are included in (b).

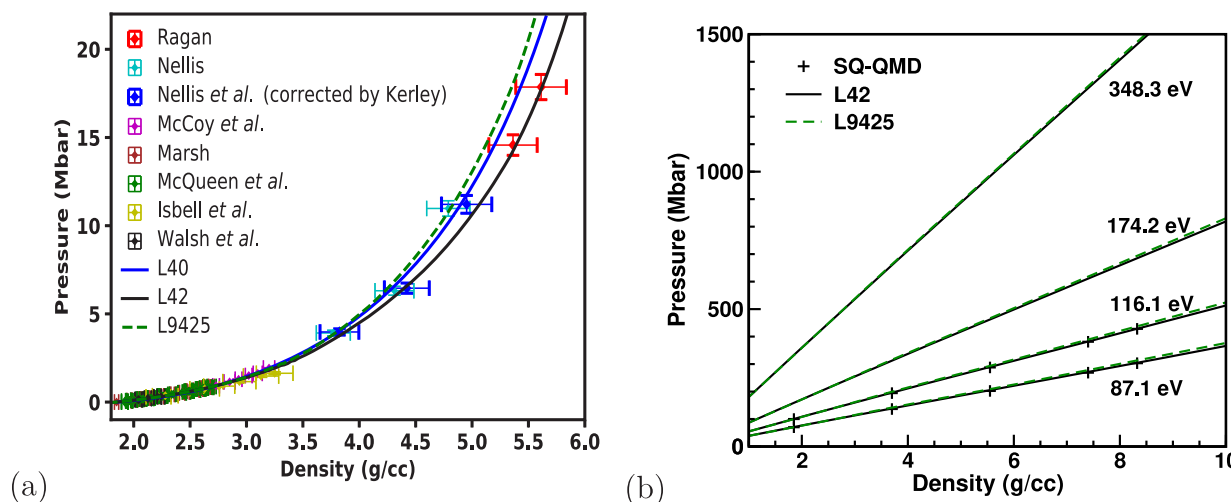


Figure 26. Comparison of L9425 with L42 on (a) the principal Hugoniot in terms of pressure vs density, with experimental data coming from various studies,^{6,78–84} and (b) high-pressure isotherms plotted alongside QMD predictions from the SQDFT code.⁶⁷

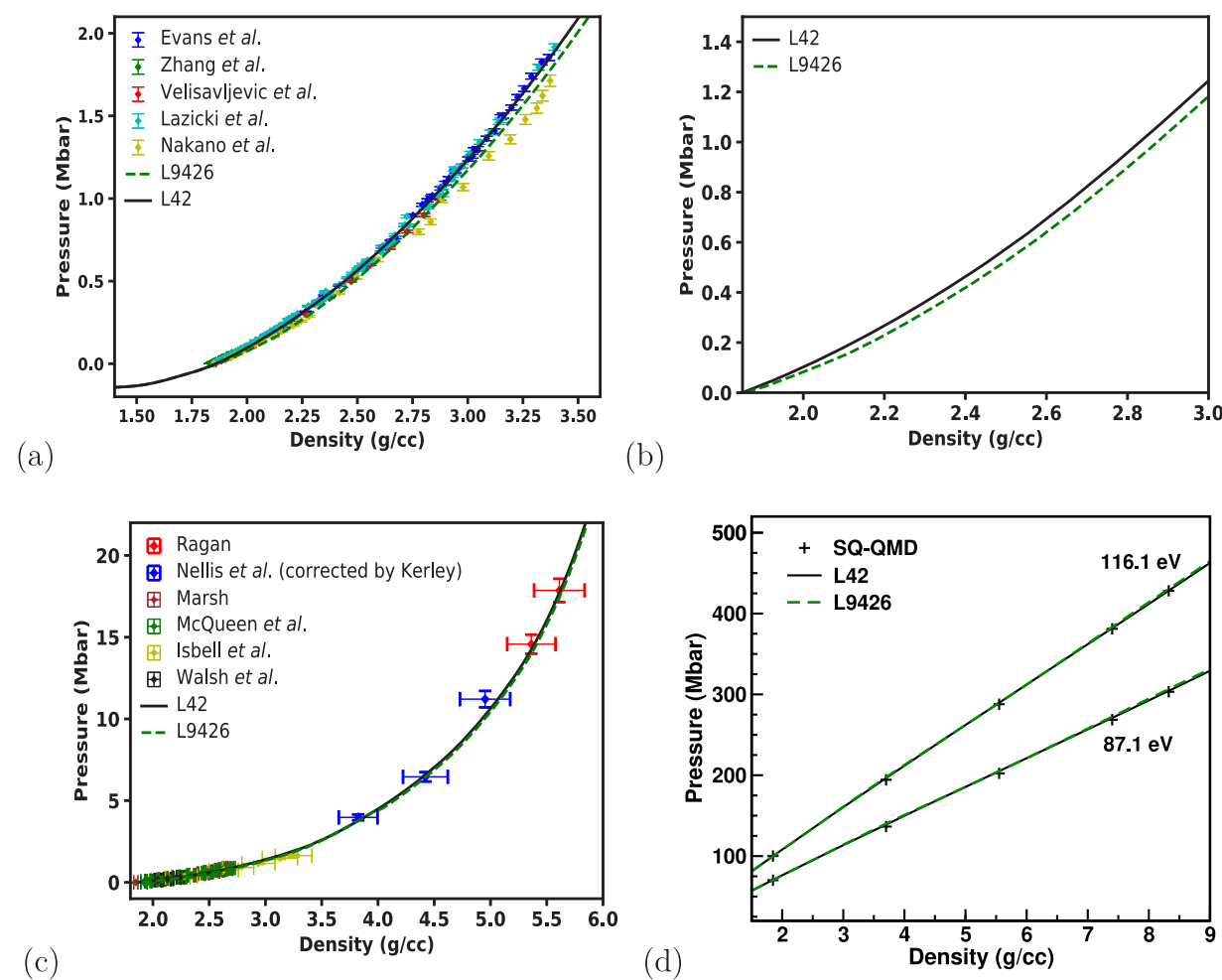


Figure 27. Comparison of our L9426 (which features a softened hcp-phase cold curve) and L42 for a variety of different properties: (a) room-temperature isotherm of the hcp phase, including experimental results;^{19,49,70,76,77} (b) the principal isentrope; (c) principal Hugoniot, including experimental results;^{6,78–84} (d) high-temperature isotherms, including QMD simulations from the SQDFT code.⁶⁷

reliable data pertaining to the melt curve are sparse, and this is especially true for pressures above 3 Mbar ($\sim \rho > 3.5 \text{ g/cm}^3$) where there is a complete absence of such data. The lack of constraints on the melt curve is evident in Figure 28a, which illustrates a wide variation in the melt temperature T_m among a

few different EOSs. Our L9427 and L9428 variations attempt to address this issue by examining the consequences of lowering and raising the melt temperature, respectively, compared to the L42 baseline. As shown in Figure 28a, our choice of T_m for L9428 is substantially higher than T_m of L42,

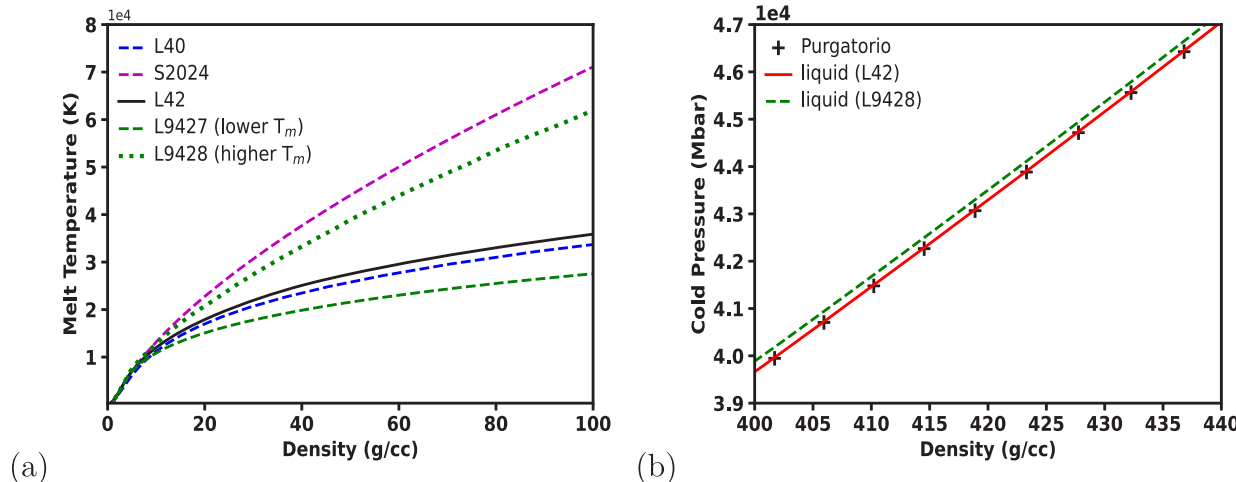


Figure 28. Comparison of L9427 and L9428 (lower and higher melt curves, respectively, for $P > 3$ Mbar) to other theoretical models: (a) melt curve from those two EOSs compared to that from our L42 baseline and the L40 and S2024 EOSs; (b) cold curve of L9428 and L42 plotted alongside predictions from Purgatorio^{26,27} at extreme conditions.

but it is closer to that of S2024, while the melt curve of L9427 is only slightly lower than that of both L42 and L40. To generate the two new melt curves while also minimizing perturbations to other known properties (e.g., the liquid Hugoniot curve), we have chosen to adjust the cold energy of the liquid rather than its ion-thermal free energy. The large perturbation to the melt curve in L9428 requires a substantial modification of the liquid cold curve. Figure 28b shows the cold curve behavior of L9428 at extremely high densities and pressures where the averaged-atom-in-jellium model of Purgatorio^{26,27,35} is expected to be accurate. Interestingly, the liquid cold curve in L9428 has been noticeably altered to the extent that, even at these extreme conditions, it does not agree with the Purgatorio predictions for the cold pressure, whereas L9427 (not shown) has a rather similar cold curve to that of L42.

CONCLUSIONS

Much like the role of an interatomic potential in classical MD simulations, an EOS provides critical input that affects the overall fidelity of hydrodynamic simulations. For a global EOS, there are five potential sources of uncertainty: (1) the inability of the EOS to match all essential constraints; (2) missing information for certain regimes that are relevant for hydrodynamic applications; (3) systematic biases associated with chosen experimental and theoretical constraints; (4) statistical uncertainties associated with selected constraints;²¹ (5) uncertainties that may be attributed to the choice of the interpolating scheme on tabular grids. In this work, we address the first three sources and have taken great care to validate the consistency of our EOS with chosen constraints. In doing so, we have obtained a global baseline EOS, L42, that reproduces known Be properties, including those at ambient conditions,⁷⁴ the principal Hugoniot,^{6,78–84} and DAC measurements.^{19,49} In addition, L42 is in close agreement with the recently reported shock-melting pressure⁷⁸ of 2.05 Mbar for Be, yielding a phase diagram that is entirely consistent with observed stability fields of the three phases considered in our study. Our EOS also obeys the correct theoretical limits at low and high densities/temperatures and provides a reasonable interpolation between these limits and the intermediate regimes where data are available. By doing so, it provides a continuous thermodynamic

function necessary for hydrodynamic simulations of ICF and other high-pressure applications.

To further improve the accuracy of the Be EOS, we have conducted *ab initio* simulations to obtain new information for two regimes that lack experimental data: (1) the bcc phase and its phase boundaries and (2) extreme temperature conditions (>87 eV) in the liquid. We have examined the effect of XCFs on bcc compression and the hcp–bcc transition boundary. Our results indicate that while compressibility is in fact sensitive to the choice of XCF, the energy differences between hcp and bcc are much less sensitive. Therefore, we have built the bcc EOS based on relative energy differences with respect to the hcp phase. This assessment allows us to constrain the hcp–bcc transition pressure to a range of 4 ± 0.5 Mbar. Together with *ab initio*-calculated thermal properties of bcc and hcp (e.g., PDOS), our baseline EOS predicts the location of the hcp–bcc–liquid triple point to be at 2.25 Mbar. For extreme temperatures, we have used the state-of-the-art SQDFT code⁶⁷ to obtain Be liquid properties. DFT simulations with this code strongly support our adoption of the recent Cell²⁴ and Purgatorio^{26,27} models to describe the ion-thermal and electron-thermal contributions, respectively, to the liquid-phase free energy. The resulting models predict a 4.4-fold compression maximum along the principal Hugoniot.

As new experimental data and theoretical calculations become available, the uncertainty and scatter in the data increase as well. In this study, we have proposed a new EOS delivery paradigm to address these issues and demonstrate this approach for Be. We have generated a set of eight variations on the baseline EOS that address different types of uncertainties arising from the choice of free-energy model, lack of constraints (absence of data for certain conditions or properties), systemic biases, or errors in experimental measurements or theoretical calculations. Statistical treatments of errors (e.g., uncertainty quantification) are not included since these approaches generally require far more data than can be extracted from conventional EOS measurements. We have shown that some uncertainties (e.g., hcp and bcc energy differences) are less important for certain applications, such as prediction of Hugoniot curves and isentropes. It is our hope that the paradigm presented in this study can be used as a way

to prioritize future scientific endeavors on Be and other materials.

AUTHOR INFORMATION

Corresponding Author

Christine J. Wu — Lawrence Livermore National Laboratory, Livermore, California 94588, United States;  orcid.org/0000-0002-2768-6415; Email: wu5@llnl.gov

Authors

Philip C. Myint — Lawrence Livermore National Laboratory, Livermore, California 94588, United States;  orcid.org/0000-0003-4383-5350

John E. Pask — Lawrence Livermore National Laboratory, Livermore, California 94588, United States

Carrie J. Prisbrey — Lawrence Livermore National Laboratory, Livermore, California 94588, United States

Alfredo A. Correa — Lawrence Livermore National Laboratory, Livermore, California 94588, United States

Phanish Suryanarayana — College of Engineering, Georgia Institute of Technology, Atlanta, Georgia 30332, United States

Joel B. Varley — Lawrence Livermore National Laboratory, Livermore, California 94588, United States;  orcid.org/0000-0002-5384-5248

Complete contact information is available at:
<https://pubs.acs.org/10.1021/acs.jpca.0c09809>

Notes

The authors declare no competing financial interest.

ACKNOWLEDGMENTS

This work was performed under the auspices of the U.S. Department of Energy by Lawrence Livermore National Laboratory under Contract DE-AC52-07NA27344. We thank M. T. Ong for his extensive assistance in manuscript preparation, L. X. Benedict for thoughtful discussions, J. R. Leek for timely implementation of MEOS modules, P. A. Sterne for help with Purgatorio, and A. Sharma for his contributions to the SQDFT code, including bug fixes and improvements that resulted in increased efficiency of the simulations. The assistance of D. R. Hamann in the construction of robust all-electron ONCV potentials is gratefully acknowledged. Allocations on the Quartz and Topaz parallel computers at LLNL employed in SQ calculations are also gratefully acknowledged.

DEDICATION

C. J. Wu would like to dedicate this article to Prof. Emily A. Carter for being an outstanding mentor and an inspirational role model: “Watching Emily, I am inspired to see the forest for the trees, to follow my curiosity for novel things, to ask the questions that matter the most, and to help others in pursuit of a better world.”

REFERENCES

- (1) Migliori, A.; Ledbetter, H.; Thoma, D. J.; Darling, T. W. Beryllium's monocrystal and polycrystal elastic constants. *J. Appl. Phys.* **2004**, *95*, 2436–2440.
- (2) Nadal, M.-H.; Bourgeois, L. Elastic moduli of beryllium versus temperature: Experimental data updating. *J. Appl. Phys.* **2010**, *108*, 033512.

(3) Cubicciotti, D. The Oxidation of Beryllium at High Temperatures. *J. Am. Chem. Soc.* **1950**, *72*, 2084–2086.

(4) Haan, S. W.; Lindl, J. D.; Callahan, D. A.; Clark, D. S.; Salmonson, J. D.; Hammel, B. A.; Atherton, L. J.; Cook, R. C.; Edwards, M. J.; Glenzer, S.; et al. Point design targets, specifications, and requirements for the 2010 ignition campaign on the National Ignition Facility. *Phys. Plasmas* **2011**, *18*, 051001.

(5) Young, D. A. *Phase Diagrams of the Elements*; University of California Press: Berkeley and Los Angeles, 1991.

(6) Kerley, G. I. *Equations of State for Be, Ni, W, and Au*; Technical Report SAND 2003-3784, 2003.

(7) Rudin, S. P.; Johnson, J. D. *Density functional theory calculations on EOS and phase stability of Be*; Technical Report LA-UR-04-7592, 2004.

(8) Benedict, L. X.; Ogitsu, T.; Trave, A.; Wu, C. J.; Sterne, P. A.; Schwegler, E. Calculations of high-pressure properties of beryllium: Construction of a multiphase equation of state. *Phys. Rev. B: Condens. Matter Mater. Phys.* **2009**, *79*, 79.

(9) Robert, G.; Legrand, P.; Bernard, S. Multiphase equation of state and elastic moduli of solid beryllium from first principles. *Phys. Rev. B: Condens. Matter Mater. Phys.* **2010**, *82*, 82.

(10) Ding, Y. H.; Hu, S. X. First-principles equation-of-state table of beryllium based on density-functional theory calculations. *Phys. Plasmas* **2017**, *24*, 062702.

(11) Martin, A.; Moore, A. The structure of beryllium, with particular reference to temperatures above 1200°C. *J. Less-Common Met.* **1959**, *1*, 85–93.

(12) Francois, M.; Contre, M. *Contribution a l'étude du diagramme pression-température du beryllium pur*. Conférence Internationale sur la Métallurgie du Beryllium. 1965; pp 201–203.

(13) Pistorius, C. W. Phase relations and structures of solids at high pressures. *Prog. Solid State Chem.* **1976**, *11*, 1–151.

(14) Ming, L. C.; Manghnani, M. H. Isothermal compression and phase transition in beryllium to 28.3 GPa. *J. Phys. F: Met. Phys.* **1984**, *14*, L1–L8.

(15) Vijayakumar, V.; Godwal, B. K.; Vohra, Y. K.; Sikka, S. K.; Chidambaram, R. On the high-pressure phase transition in beryllium metal. *J. Phys. F: Met. Phys.* **1984**, *14*, L65–L68.

(16) Luo, F.; Cai, L.-C.; Chen, X.-R.; Jing, F.-Q.; Alfè, D. Ab initio calculation of lattice dynamics and thermodynamic properties of beryllium. *J. Appl. Phys.* **2012**, *111*, 053503.

(17) Song, H.-F.; Liu, H.-F. Modified mean-field potential approach to thermodynamic properties of a low-symmetry crystal: Beryllium as a prototype. *Phys. Rev. B: Condens. Matter Mater. Phys.* **2007**, *75*, 75.

(18) Evans, W. J.; Cynn, H.; Lazicki, A.; Yoo, C. S.; Ohishi, Y.; Sata, N. *High-Pressure/High-Temperature Studies of the Low-Z. materials - Beryllium*; Technical Report UCRL-TR-219496, 2006.

(19) Lazicki, A.; Dewaele, A.; Loubeire, P.; Mezouar, M. High-pressure-temperature phase diagram and the equation of state of beryllium. *Phys. Rev. B: Condens. Matter Mater. Phys.* **2012**, *86*, 174118.

(20) Lu, Y.; Sun, T.; Zhang, P.; Zhang, P.; Zhang, D.-B.; Wentzcovitch, R. Premelting hcp to bcc Transition in Beryllium. *Phys. Rev. Lett.* **2017**, *118*, 118.

(21) Ali, S. J.; Swift, D. C.; Wu, C. J.; Kraus, R. G. Development of uncertainty-aware equation-of-state models: Application to copper. *J. Appl. Phys.* **2020**, *128*, 185902.

(22) More, R. M.; Warren, K. H.; Young, D. A.; Zimmerman, G. B. A new quotidian equation of state (QEoS) for hot dense matter. *Phys. Fluids* **1988**, *31*, 3059.

(23) Cranfill, C. W.; More, R. M. *IONEOS: A Fast, Analytic, Ion Equation-of-State Routine*; Technical Report LA-7313-MS, 1978.

(24) Correa, A.; Benedict, L.; Morales, M.; Sterne, P.; Castor, J.; Schwegler, E. A first-principles global multiphase equation of state for hydrogen. 2018; unpublished; arXiv:1806.01346 [pdf, other].

(25) Benedict, L. X.; Driver, K. P.; Hamel, S.; Militzer, B.; Qi, T.; Correa, A. A.; Saul, A.; Schwegler, E. Multiphase equation of state for carbon addressing high pressures and temperatures. *Phys. Rev. B: Condens. Matter Mater. Phys.* **2014**, *89*, 89.

- (26) Wilson, B.; Sonnad, V.; Sterne, P.; Isaacs, W. Purgatorio – A new implementation of the Inferno algorithm. *J. Quant. Spectrosc. Radiat. Transfer* **2006**, *99*, 658–679.
- (27) Sterne, P. A.; Hansen, S. B.; Wilson, B. G.; Isaacs, W. A. Equation of state, occupation probabilities and conductivities in the average atom Purgatorio code. *High Energy Density Phys.* **2007**, *3*, 278–282.
- (28) Fritsch, F. N. *The LEOS Interpolation Package*; Technical Report UCRL-ID-148554-REV-1, 2003; 30 pp.
- (29) Brown, J. M. Local basis function representations of thermodynamic surfaces: Water at high pressure and temperature as an example. *Fluid Phase Equilib.* **2018**, *463*, 18–31.
- (30) Brown, J. M.; Journaux, B. Local-Basis-Function Equation of State for Ice VII-X to 450 GPa at 300 K. *Minerals* **2020**, *10*, 92.
- (31) Vinet, P.; Rose, J. H.; Ferrante, J.; Smith, J. R. Universal features of the equation of state of solids. *J. Phys.: Condens. Matter* **1989**, *1*, 1941–1963.
- (32) Kittel, C. *Introduction to Solid State Physics*; John Wiley and Sons, Inc., 1986.
- (33) Chisolm, E. D.; Wallace, D. C. Dynamics of monatomic liquids. *J. Phys.: Condens. Matter* **2001**, *13*, R739–R769.
- (34) Wallace, D. C.; Chisolm, E. D.; Bock, N.; Lorenzi-Venneri, G. D. Statistical mechanics model for the transit free energy of monatomic liquids. *Phys. Rev. E* **2010**, *81*, 041201.
- (35) Swift, D. C.; Lockard, T.; Smith, R. F.; Wu, C. J.; Benedict, L. X. High pressure melt curve of iron from atom-in-jellium calculations. *Phys. Rev. Res.* **2020**, *2*, 023034.
- (36) Young, D. A.; Corey, E. M. A new global equation of state model for hot, dense matter. *J. Appl. Phys.* **1995**, *78*, 3748–3755.
- (37) Wu, C. J.; Young, D. A.; Sterne, P. A.; Myint, P. C. Equation of state for a chemically dissociative, polyatomic system: Carbon dioxide. *J. Chem. Phys.* **2019**, *151*, 224505.
- (38) Sears, F.; Salinger, G.; Lee, J. *Thermodynamics, Kinetic Theory, and Statistical Thermodynamics*; Addison-Wesley Principles of Physics series; Addison-Wesley Publishing Company, 1975.
- (39) Noulez, A.; Vergassola, M. A fast Legendre transform algorithm and applications to the adhesion model. *Journal of Scientific Computing* **1994**, *9*, 259–281.
- (40) Corrias, L. Fast Legendre–Fenchel Transform and Applications to Hamilton–Jacobi Equations and Conservation Laws. *SIAM Journal on Numerical Analysis* **1996**, *33*, 1534–1558.
- (41) Lucet, Y. Faster than the Fast Legendre Transform, the Linear-time Legendre Transform. *Numerical Algorithms* **1997**, *16*, 171–185.
- (42) McMahan, A. K. The α - β transition in $T = 0$ high pressure beryllium. *AIP Conf. Proc.* **1982**, *78*, 340–344.
- (43) Lam, P. K.; Chou, M. Y.; Cohen, M. L. Temperature- and pressure-induced crystal phase transitions in Be. *J. Phys. C: Solid State Phys.* **1984**, *17*, 2065–2073.
- (44) Meyer-ter-Vehn, J.; Zittel, W. Electronic structure of matter at high compression: Isostructural transitions and approach of the Fermi-gas limit. *Phys. Rev. B: Condens. Matter Mater. Phys.* **1988**, *37*, 8674–8688.
- (45) Palanivel, B.; Rao, R. S.; Godwal, B. K.; Sikka, S. K. On the relative stability of orthorhombic and hcp phases of beryllium at high pressures. *J. Phys.: Condens. Matter* **2000**, *12*, 8831–8836.
- (46) Ceperley, D. M.; Alder, B. J. Ground State of the Electron Gas by a Stochastic Method. *Phys. Rev. Lett.* **1980**, *45*, 566–569.
- (47) Perdew, J. P.; Burke, K.; Ernzerhof, M. Generalized Gradient Approximation Made Simple. *Phys. Rev. Lett.* **1996**, *77*, 3865–3868.
- (48) Hammer, B.; Hansen, L. B.; Nørskov, J. K. Improved adsorption energetics within density-functional theory using revised Perdew–Burke–Ernzerhof functionals. *Phys. Rev. B: Condens. Matter Mater. Phys.* **1999**, *59*, 7413–7421.
- (49) Evans, W. J.; Lipp, M. J.; Cynn, H.; Yoo, C. S.; Somayazulu, M.; Häusermann, D.; Shen, G.; Prakapenka, V. X-ray diffraction and Raman studies of beryllium: Static and elastic properties at high pressures. *Phys. Rev. B: Condens. Matter Mater. Phys.* **2005**, *72*, 72.
- (50) Perdew, J. P.; Ruzsinszky, A.; Csonka, G. I.; Vydrov, O. A.; Scuseria, G. E.; Constantin, L. A.; Zhou, X.; Burke, K. Restoring the Density-Gradient Expansion for Exchange in Solids and Surfaces. *Phys. Rev. Lett.* **2008**, *100*, 136406.
- (51) Perdew, J. P.; Wang, Y. Accurate and simple analytic representation of the electron-gas correlation energy. *Phys. Rev. B: Condens. Matter Mater. Phys.* **1992**, *45*, 13244–13249.
- (52) Zhang, Y.; Yang, W. Comment on “Generalized Gradient Approximation Made Simple”. *Phys. Rev. Lett.* **1998**, *80*, 890–890.
- (53) Heyd, J.; Scuseria, G. E.; Ernzerhof, M. Hybrid functionals based on a screened Coulomb potential. *J. Chem. Phys.* **2003**, *118*, 8207–8215.
- (54) Heyd, J.; Scuseria, G. E.; Ernzerhof, M. Erratum: “Hybrid functionals based on a screened Coulomb potential” [J. Chem. Phys. **118**, 8207 (2003)]. *J. Chem. Phys.* **2006**, *124*, 219906.
- (55) Klimeš, J.; Bowler, D. R.; Michaelides, A. Chemical accuracy for the van der Waals density functional. *J. Phys.: Condens. Matter* **2010**, *22*, 022201.
- (56) Lee, K.; Murray, É. D.; Kong, L.; Lundqvist, B. I.; Langreth, D. C. Higher-accuracy van der Waals density functional. *Phys. Rev. B: Condens. Matter Mater. Phys.* **2010**, *82*, 82.
- (57) Armiento, R.; Mattsson, A. E. Functional designed to include surface effects in self-consistent density functional theory. *Phys. Rev. B: Condens. Matter Mater. Phys.* **2005**, *72*, 72.
- (58) Mattsson, A. E.; Armiento, R.; Paier, J.; Kresse, G.; Wills, J. M.; Mattsson, T. R. The AM05 density functional applied to solids. *J. Chem. Phys.* **2008**, *128*, 084714.
- (59) Mattsson, A. E.; Armiento, R. Implementing and testing the AM05 spin density functional. *Phys. Rev. B: Condens. Matter Mater. Phys.* **2009**, *79*, 79.
- (60) Monkhorst, H. J.; Pack, J. D. Special points for Brillouin-zone integrations. *Phys. Rev. B* **1976**, *13*, 5188–5192.
- (61) Lindl, J. Development of the indirect-drive approach to inertial confinement fusion and the target physics basis for ignition and gain. *Phys. Plasmas* **1995**, *2*, 3933–4024.
- (62) Suryanarayana, P. $O(N)$ spectral quadrature for linear-scaling Density Functional Theory. *Chem. Phys. Lett.* **2013**, *584*, 182–187.
- (63) Pratapa, P. P.; Suryanarayana, P.; Pask, J. E. Spectral Quadrature method for accurate $O(N)$ electronic structure calculations of metals and insulators. *Comput. Phys. Commun.* **2016**, *200*, 96–107.
- (64) Suryanarayana, P. On nearsightedness in metallic systems for $O(N)$ Density Functional Theory calculations: A case study on aluminum. *Chem. Phys. Lett.* **2017**, *679*, 146–151.
- (65) Haydock, R.; Heine, V.; Kelly, M. J. Electronic structure based on the local atomic environment for tight-binding bands. *J. Phys. C: Solid State Phys.* **1972**, *5*, 2845–2858.
- (66) Goedecker, S.; Colombo, L. Efficient Linear Scaling Algorithm for Tight-Binding Molecular Dynamics. *Phys. Rev. Lett.* **1994**, *73*, 122–125.
- (67) Suryanarayana, P.; Pratapa, P. P.; Sharma, A.; Pask, J. E. SQDFT: Spectral Quadrature method for large-scale parallel $O(N)$ Kohn–Sham calculations at high temperature. *Comput. Phys. Commun.* **2018**, *224*, 288–298.
- (68) Sharma, A.; Hamel, S.; Bethkenhagen, M.; Pask, J. E.; Suryanarayana, P. Real-space formulation of the stress tensor for $O(N)$ density functional theory: Application to high temperature calculations. *J. Chem. Phys.* **2020**, *153*, 034112.
- (69) Hamann, D. R. Optimized norm-conserving Vanderbilt pseudopotentials. *Phys. Rev. B: Condens. Matter Mater. Phys.* **2013**, *88*, 085117.
- (70) Zhang, S.; Lazicki, A.; Militzer, B.; Yang, L. H.; Caspersen, K.; Gaffney, J. A.; Däne, M. W.; Pask, J. E.; Johnson, W. R.; Sharma, A.; et al. Equation of state of boron nitride combining computation, modeling, and experiment. *Phys. Rev. B: Condens. Matter Mater. Phys.* **2019**, *99*, 99.
- (71) Perdew, J. P.; Zunger, A. Self-interaction correction to density-functional approximations for many-electron systems. *Phys. Rev. B: Condens. Matter Mater. Phys.* **1981**, *23*, 5048–5079.

- (72) Minary, P.; Martyna, G. J.; Tuckerman, M. E. Algorithms and novel applications based on the isokinetic ensemble. II. Ab initio molecular dynamics. *J. Chem. Phys.* **2003**, *118*, 2527.
- (73) Eliezer, S.; Ghatak, A.; Hora, H.; Teller, E. *Fundamentals of Equations of State*; World Scientific, 2002.
- (74) *Chemistry WebBook*; National Institute of Standards and Technology (NIST), 2020; <https://webbook.nist.gov/chemistry/>.
- (75) Rumble, J. R., Ed. Density of Molten Elements and Salts. *CRC Handbook of Chemistry and Physics*, 101st ed.; CRC Press/Taylor and Francis: Boca Raton, FL, 2020.
- (76) Velisavljevic, N.; Chesnut, G. N.; Vohra, Y. K.; Weir, S. T.; Malba, V.; Akella, J. Structural and electrical properties of beryllium metal to 66 gpa studied using designer diamond anvils. *Phys. Rev. B: Condens. Matter Mater. Phys.* **2002**, *65* (17), 172107.
- (77) Nakano, K.; Akahama, Y.; Kawamura, H. X-ray diffraction study of Be to megabar pressure. *J. Phys.: Condens. Matter* **2002**, *14*, 10569–10573.
- (78) McCoy, C. A.; Knudson, M. D.; Desjarlais, M. P. Sound velocity, shear modulus, and shock melting of beryllium along the Hugoniot. *Phys. Rev. B: Condens. Matter Mater. Phys.* **2019**, *100*, 100.
- (79) Nellis, W. J.; Moriarty, J. A.; Mitchell, A. C.; Holmes, N. C. Equation of state of beryllium at shock pressures of 0.4–1.1 TPa (4–11 Mbar). *J. Appl. Phys.* **1997**, *82*, 2225–2227.
- (80) Ragan, C. E. Shock compression measurements at 1 to 7 TPa. *Phys. Rev. A: At., Mol., Opt. Phys.* **1982**, *25*, 3360–3375.
- (81) Marsh, S. P., Ed. *LASL Shock Hugoniot Data*; University of California Press, 1980.
- (82) McQueen, R. G.; Marsh, S. P.; Taylor, J. W.; Fritz, J. N.; Carter, W. J. In *High-Velocity Impact Phenomena*; Kinslow, R., Ed.; Academic Press: New York, 1970; Chapter The Equation of State of Solids from Shock Wave Studies, pp 293–417, 521–568, Library of Congress Catalog Card Number: 71-91425.
- (83) Isbell, W. M.; Shipman, F. H.; Jones, A. H. *Hugoniot Equation of State Measurements for Eleven Materials to Five Megabars*; Department of the Army, 1968.
- (84) Walsh, J. M.; Rice, M. H.; McQueen, R. G.; Yarger, F. L. Shock-Wave Compressions of Twenty-Seven Metals. Equations of State of Metals. *Phys. Rev.* **1957**, *108*, 196–216.
- (85) Cauble, R.; Perry, T. S.; Bach, D. R.; Budil, K. S.; Hammel, B. A.; Collins, G. W.; Gold, D. M.; Dunn, J.; Celliers, P.; Silva, L. B. D.; et al. Absolute Equation-of-State Data in the 10–40 Mbar (1–4 TPa) Regime. *Phys. Rev. Lett.* **1998**, *80*, 1248–1251.
- (86) Knudson, M. D. Megaamps, megagauss, and megabars: Using the Sandia Z Machine to perform extreme material dynamics experiments. *AIP Conf. Proc.* **2011**, *1426*, 35–42.
- (87) Hao, A.; Zhu, Y. First-principle investigations of structural stability of beryllium under high pressure. *J. Appl. Phys.* **2012**, *112*, 023519.
- (88) Dewaele, A.; Loubeyre, P.; Occelli, F.; Marie, O.; Mezouar, M. Toroidal diamond anvil cell for detailed measurements under extreme static pressures. *Nat. Commun.* **2018**, *9*, 2913.
- (89) Lindemann, F. A. The calculation of molecular vibration frequencies. *Phys. Z.* **1910**, *11*, 609–612. (in German).

■ NOTE ADDED AFTER ASAP PUBLICATION

This paper was originally published ASAP on February 15, 2021. Due to a production error, reference 1 was mistakenly replaced. The corrected version was reposted on February 15, 2021.